DTIC FILE COPY

(2)

REPORT DOCUMENTATION PAGE

Form Approved
OMB No. 0704-0188

AD-A217 776

1. AGENCY USE ONLY (Leave blank)	2. REPORT DATE	3. REPORT TYPE AND DATES COVERED
	July 89	Final Technical 1 Aug 88 - 31 Jan 89

4. TITLE AND SUBTITLE

Superconductive Microprobes for Eddy Current Evaluation of Materials

5. FUNDING NUMBERS

F49620-88-C-0091

6. AUTHOR(S)

Dr Walter N. Podney

7. PERFORMING ORGANIZATION NAME(S) AND ADDRESS(ES)

Physical Dynamics, Inc
7855 Fay Avenue, Suite 300
La Jolla, CA 92037

8. PERFORMING ORGANIZATION REPORT NUMBER

AFOSR-TR- 90-0011

9. SPONSORING/MONITORING AGENCY NAME(S) AND ADDRESS(ES)

Dr Harold Weinstock
AFOSR/NE
Bldg 410
Bolling AFB DC 20332-6448

10. SPONSORING/MONITORING AGENCY REPORT NUMBER

11. SUPPLEMENTARY NOTES

DTIC
ELECTE
FEB 07 1990
B D

12a. DISTRIBUTION/AVAILABILITY STATEMENT

Approved for public release
distribution unlimited

12b. DISTRIBUTION CODE

13. ABSTRACT (Maximum 200 words)

Superconductive quantum interference devices (SQUIDs) offer new technology for locating materials flaws electromagnetically that promises to increase sensitivity, depth of magnetic flux enables use of microscopic pickup loops in a gradiometer configuration to give high resolution. A cryogenic umbilical connects pickup loops to a remote cryostat housing SQUID sensors to ease scanning. A pair of drive coils a few millimeters in radius that encircle pickup loops forming a coplanar gradiometer 1 mm or less in radius comprise a superconductive microprobe. It provides a depth of field of several millimeters to a 0.1 mm flaw in an aluminum plate, when operating with a drive current a 1 A oscillating at a frequency of 1kHz. Its field of view ranges to several millimeters, for flaws a few millimeters deep, and its horizontal resolution is 1 mm or so, for flaw depths out to its depth of field. An array of microprobes form receptors much like rods in the retina of a magnetic eye. The eye leads to an electromagnetic microscope for imaging internal flaws in aluminum plates. It gives multiple images that enable resolving depth of a 0.1 mm flaw to a few tenths of a millimeter with a horizontal resolution of one millimeter or so. (ICR)

14. SUBJECT TERMS	15. NUMBER OF PAGES
	16. PRICE CODE

17. SECURITY CLASSIFICATION OF REPORT	18. SECURITY CLASSIFICATION OF THIS PAGE	19. SECURITY CLASSIFICATION OF ABSTRACT	20. LIMITATION OF ABSTRACT
UNCLASSIFIED	UNCLASSIFIED	UNCLASSIFIED	UNLIMITED

SUPERCONDUCTIVE MICROPROBES FOR EDDY CURRENT EVALUATION OF MATERIALS

by

Walter N. Podney

Report Number PD–LJ–89–370R

Phase I Final Report
Department of the Air Force Contract F49620–88–C–0091

Submitted to:

Air Force Office of Scientific Research
Directorate of Electronic and Material Sciences
Dr. Harold Weinstock, Program Manager

Submitted by:

Physical Dynamics, Inc.
7855 Fay Avenue, Suite 300
La Jolla, California 92037

July 1989

SUMMARY

Superconductive quantum interference devices (SQUIDs) offer new technology for locating material flaws electromagnetically that promises to increase sensitivity, depth of field, and field of view and to enhance resolution. The ultrahigh sensitivity of SQUIDs to magnetic flux enables use of microscopic pickup loops in a gradiometer configuration to give high resolution. A cryogenic umbilical connects pickup loops to a remote cryostat housing SQUID sensors to ease scanning.

A pair of drive coils a few millimeters in radius that encircle pickup loops forming a coplanar gradiometer 1 mm or less in radius comprise a superconductive microprobe. It provides a depth of field of several millimeters to a 0.1 mm flaw in an aluminum plate, when operating with a drive current of 1 A oscillating at a frequency of 1 kHz. Its field of view ranges to several millimeters, for flaws a few millimeters deep, and its horizontal resolution is 1 mm or so, for flaw depths out to its depth of field.

An array of microprobes form receptors much like rods in the retina of a magnetic eye. The eye leads to an electromagnetic microscope for imaging internal flaws in aluminum plates. It gives multiple images that enable resolving depth of a 0.1 mm flaw to a few tenths of a millimeter with a horizontal resolution of one millimeter or so.

TABLE OF CONTENTS

1.0	INTRODUCTION	1
2.0	CONFIGURATIONS OF A MICROPROBE	2
	2.1 Receiver Loops	2
	2.1.2 Second Order Gradiometer	5
	2.1.3 Third Order Gradiometer	5
	2.1.4 Fourth Order Gradiometer	5
	2.2 Source Coils	6
3.0	FLAW SIGNAL DESCRIPTION	7
	3.1 Induced Eddy Currents	7
	3.2 Eddy Current Perturbation	9
	3.3 Magnetic Flux Perturbation	10
	3.4 Elemental Flaw Signal	11
4.0	MICROPROBE RESPONSE TO A FLAW	12
	4.1 Response of a Second Order Microporbe	13
	4.2 Response of a Fourth Order Microprobe	17
5.0	ELECTROMAGNETIC MICROSCOPE	21
	5.1 Elements of a Magnetic Eye	21
	5.2 Depth of Field	21
	5.3 Field of View	23
	5.4 Resolution	23
6.0	ASSESSMENT OF FEASIBILITY AND TECHNICAL RISK	29
	6.1 Feasibility	29
	6.2 Technical Risk	30
7.0	CONCLUSION	32
8.0	REFERENCES	33
	APPENDIX	
	A. EDDY CURRENTS IN A UNIFORMLY CONDUCTING HALF–SPACE FROM AN ELECTRIC CURRENT OSCILLATING IN A CIRCULAR LOOP	A1
	B. MUTUAL INDUCTANCES OF COAXIAL LOOPS ABOVE A CONDUCTING HALF–SPACE	B1
	C. RECIPROCITY RELATION	C1

1.0 INTRODUCTION

Superconductive quantum interference devices (SQUIDs) offer new technology for locating material flaws electromagnetically that promises to increase sensitivity and depth of field, to enhance resolution, and to enable multivariate measurements with a single system. They can measure changes in magnetic flux as small as 10^{-4} flux quanta (a flux quantum is 2.07×10^{-15} Tm^2) at frequencies from 0.1 Hz to several kilohertz. A conventional pickup coil, operating at 5 MHz with a sensitivity of 1 μV, requires about 10^5 turns of wire to give an equal flux sensitivity, or alternatively a 100 turn coil must operate at a frequency of 5 GHz, which is equally impractical. A SQUID, however, needs but a single loop one millimeter in diameter.

The ultrahigh sensitivity of SQUIDs to magnetic flux allows use of microscopic pickup loops in a gradiometer configuration to give high resolution. Arrays of closely spaced loops can provide high scan rates and image flawed regions. High sensitivity also allows operating at standoff distances of several millimeters, which increases aperture and hence scan rate. Surveys can be made rapidly at large standoff and low resolution followed by mapping flawed regions at small standoff and high resolution.

Because their sensitivity is independent of frequency over a wide range, SQUIDs enable using low frequencies to increase depth of field as well as operating at multiple frequencies to scan over depth. They also can measure minute magnetic inhomogeneities of a material and so evaluate magnetic properties such as remanent magnetization, magnetic permeability, coercive field strength, and Barkhausen noise. The full range of measurements of magnetic and electrical properties available provides the versatility of *multivariate measurements with a single system.*

Phase I research reported here uses model analyses to quantify advances anticipated from using SQUID technology for nondestructive evaluation of materials. It demonstrates feasiblity of the design of an eddy current probe that uses microscopic, coplanar pickup loops in a gradiometer configuraton to attain a resolution of one millimeter and a depth of field of several millimeters to a 0.1 mm flaw in an aluminum plate, at operating frequencies from a few hundred to a few thousand Hertz. The design leads to an array of closely spaced microprobes suited to scanning plates and tubes rapidly and with high resolution.

To realize the concept of a microscopic probe, we set forth an innovative cryogenic design that attaches the probe to a compact cryostat, housing SQUID sensors, through an umbilical formed by a cryogenic heat pipe. A cluster of microprobes forms an array much like rods in the retina of a magnetic eye. The eye leads to an electromagnetic microscope the gives multiple images of internal flaws, allowing resolution in depth of a few tenths of a millimeter to a 0.1 mm flaw and a horizontal resolution of 1 mm or so.

2.0 CONFIGURATIONS OF A MICROPROBE

Figure 2.1 shows a configuration of source coils and pickup loops that comprise a microprobe. They form a coplanar nest of concentric circles. The two outermost coils carry an oscillating electric current to drive eddy currents. Current in the inner drive coil opposes current in the outer coil in order to suppress interference from the source at the receiver, formed by the inner most loops. Loops of the receiver wind oppositely to form a planar gradiometer of order n, where n is the number of loops. Figure 2.2 shows receiver windings divided into pairs of opposing quadrants to form a biaxial gradiometer of order n.

We first specify geometry of receiver loops forming a gradiometer of order n and then give specifications of source coils.

2.1 RECEIVER LOOPS

Receiver loops form a planar gradiometer of order n, where n is the number of pickup loops. A loop has N_i turns and radius r_i. For axial symmetry, the vector potential, $\vec{A}$, of a magnetic flux density, $\vec{B} = \vec{\nabla} \times \vec{A}$, threading the loops points in the direction $\hat{\phi}$ of cylindrical coordinates r, ϕ, and z, where $\hat{z}$ points along the common axis of the loops. The expression

$$A_{\varphi}(r) = \sum_{n=1}^{\infty} C_n r^n \tag{2.1a}$$

expands magnitude of the vector potential in powers of the radial coordinate r. For example, a magnetic dipole, $M\hat{z}$, at position z along the $\hat{z}$ axis gives an expansion expressed by the relation

$$A_{\varphi}(r) = \frac{\mu_0 M r}{4\pi z^3} \sum_{n=0}^{\infty} \frac{(2n+1)!!}{(2n)!!} \left[\frac{r}{z}\right]^{2n} , \tag{2.1b}$$

where $\mu_0 = 4\pi \times 10^{-7}$ H/m and double factorials denote products of odd and even integers.

The magnetic flux threading an ith loop is $2\pi r_i N_i A_{\varphi}(r_i)$, so Equation 2.1a says that the relation

$$R_m = \sum_{i=1}^{m} N_i 2\pi \sum_{n=1}^{\infty} C_n (r_i)^{n+1} \tag{2.2a}$$

gives the net flux, R_m, threading a receiver formed by m concentric loops with $r_{i-1} > r_i > 0$. The net flux or response R_m vanishes to order r^m for a gradiometer of m*th* order, so Equation 2.2a tells us that the relations

$$\sum_{i=1}^{m} N_i (r_i)^{n+1} = 0 \text{ , for } n = 1, 2, 3, .., m-1, \tag{2.2b}$$

specify ratios of radii and number of turns of its m concentric loops.

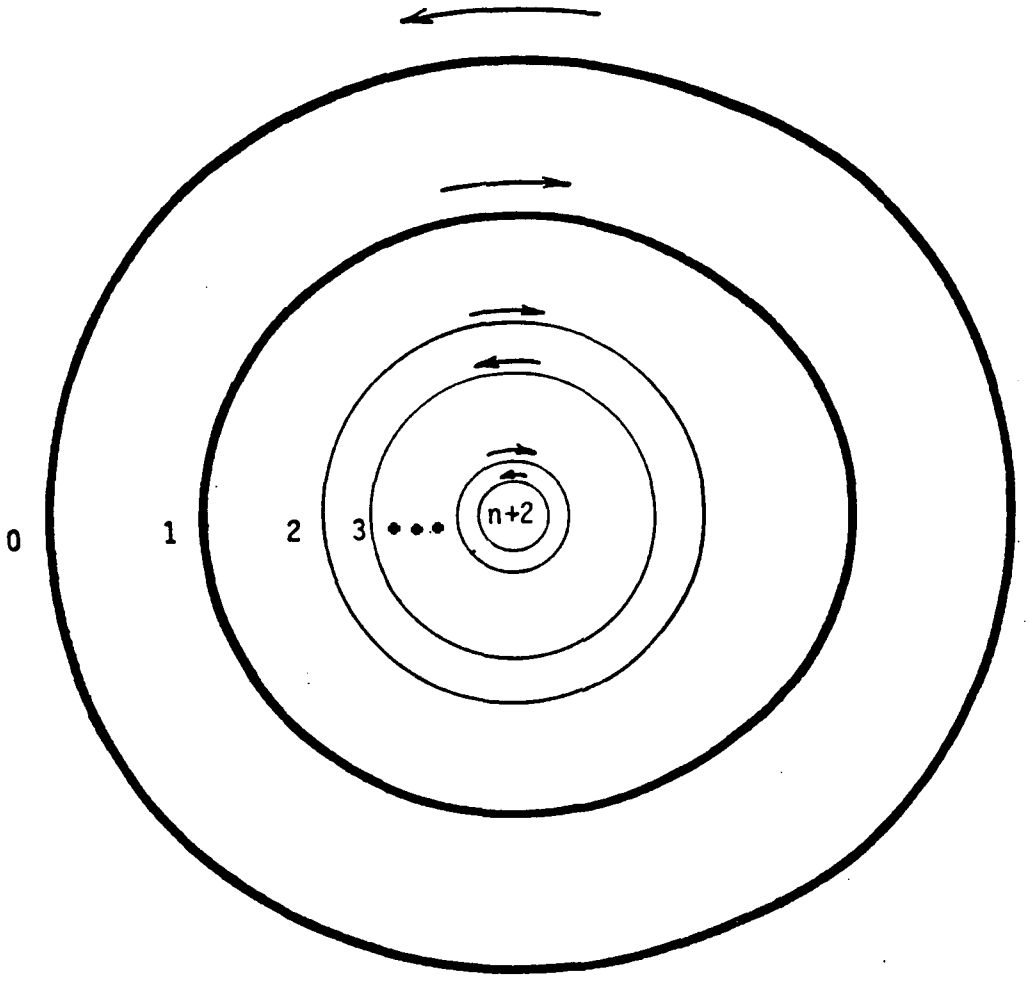

Figure 2.1

A coplanar nest of drive coils and pickup loops forming a planar gradiometer of order n. The two outermost loops, numbered 0 and 1, are drive coils that carry an oscillating current to excite eddy currents. Their currents flow oppositely, as marked by arrows, in order to null interference from drive currents at the receiver, formed by n innermost loops, numbered 2 through 2+n. Arrows show that they wind oppositely in order to give a null response to magnetic fields radially uniform to order n–2. Triple dots, $\cdots$, between receiver loops denote continuation of windings to loop n+2 .

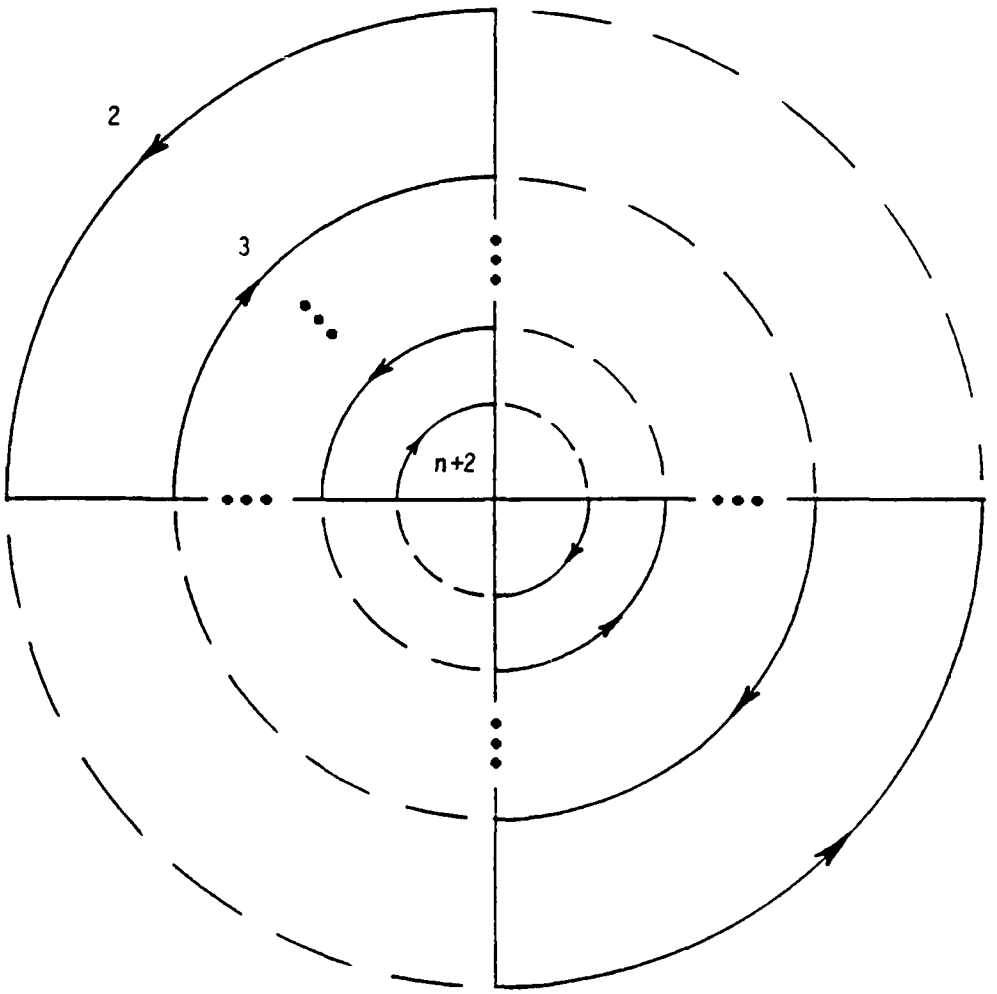

Figure 2.2

Receiver pickup loops forming a planar, biaxial gradiometer of order n. Opposite quadrants form pickup loops of an axis, as marked by heavy lines. Dashed lines mark pickup loops of the second axis. Arrows show winding of adjacent loops is opposite. Closures for each loop run parallel along diameters, and crossovers are at the center. Triple dots, $\cdots$, between loops denote continuation of windings to loop n+2 .

2.1.2 Second Order Gradiometer

For a gradiometer of second order, m = 2, and Equation 2.2b gives the relation

$$N_1 r_1^2 + N_2 r_2^2 = 0 \tag{2.3}$$

that specifies the ratio of radii and number of turns of the two loops. Namely, $N_2 r_2^2 = -1$, for $r_1 = 1$ and $N_1 = 1$. (Number of turns is positive for a right handed winding and negative for a left handed winding.) Equation 2.1b then tells us that response of a second order gradiometer to a dipole at position z on the axis is proportional to z^{-5}, to lowest order.

2.1.3 Third Order Gradiometer

For a gradiometer of third order, m = 3, and the relations

$$1 + N_2 r_2^2 + N_3 r_3^2 = 0 \tag{2.4a}$$

and

$$1 + N_2 r_2^3 + N_3 r_3^3 = 0 \tag{2.4b}$$

constrain number of turns and radii of the two innermost loops, with $N_1 = 1$ and $r_1 = 1$. For $N_2 = -2$ and $N_3 = 2$, Equations 2.4a and 2.4b require $r_2 = 0.8405$ and $r_3 = 0.4542$.

Response to a dipole on the axis is again proportional to z^{-5}, to lowest order, for a gradiometer of third order, because the response to a dipole contains even powers of r alone.

2.1.4 Fourth Order Gradiometer

For a gradiometer of fourth order, m = 4, and Equation 2.2b gives the relations

$$1 + N_2 r_2^2 + N_3 r_3^2 + N_4 r_4^2 = 0 , \tag{2.5a}$$

$$1 + N_2 r_2^3 + N_3 r_3^3 + N_4 r_4^3 = 0 , \tag{2.5b}$$

and

$$1 + N_2 r_2^4 + N_3 r_3^4 + N_4 r_4^4 = 0 , \tag{2.5c}$$

that constrain number of turns and radii of the three innermost loops, for $N_1 = 1$ and $r_1 = 1$. For $N_2 = -2$, $N_3 = 2$, and $N_4 = -2$, they require $r_2 = 0.899253$, $r_3 = 0.635352$, and $r_4 = 0.308249$.

Equation 2.1b tells us that response to a dipole on the axis is proportional to z^{-7}, to lowest order, for a gradiometer of fourth order.

2.2 SOURCE COILS

The source comprises two coplanar coils that encircle the receiver. Electric current oscillating in the inner coil opposes current in the outer coil in order to suppress interference from the source at the receiver. Current, I_1, in the inner coil balances current in the outer coil, I_0, so interference from the source vanishes. We set the current so that $I_1 = -\beta I_0$, where β is a balance factor.

The balance factor β depends on mutual inductances, $M_{ij}(h)$, between source loops, numbered 0 and 1, and receiver loops, numbered 2 through m + 2, as expressed by the relation

$$\beta = \frac{M_{02}(h) + M_{03}(h) + \cdots + M_{0n}}{M_{12}(h) + M_{13}(h) + \cdots + M_{1n}} , \qquad (2.6a)$$

with n = m + 2. Here, the expression (Appendix B, Equation B4.a)

$$M_{ij}(h) = \mu_0 \pi N_i r_i N_j r_j \int_0^\infty \left[1 + \frac{(1-\gamma/k)}{(1+\gamma/k)} e^{-2kh} \right] J_1(kr_i) J_1(kr_j) \, dk \qquad (2.6b)$$

gives the mutual inductance between coplanar, concentric loops of radii r_i and r_j at height h above an electrically conducting plate, where $\gamma^2 = k^2 + i\mu_0\sigma\omega$, σ is electrical conductivity of the plate, ω is the carrier frequency, $\mu_0 = 4\pi \times 10^{-7}$ H/m, and $J_1(x)$ is a Bessel function of the first kind and order one.

We choose the number of turns and radius, N_1 and r_1, of the inner drive coil so that β is unity far above the plate ($h \gg 0$) and/or at low frequency ($\gamma \approx k$), where the exponential term in Equation 2.6b vanishes. The expression (Appendix B, Equation B4.c)

$$\lim_{\omega \to 0} M_{ij} = M_{ij}^{00} = \mu_0 N_i N_j \left[(r_i^2 + r_j^2) K(\rho_{ij}^0) - (r_i + r_j)^2 E(\rho_{ij}^0) \right] \qquad (2.7a)$$

then gives mutual inductances, where $K(\rho)$ and $E(\rho)$ are complete elliptic integrals of the first and second kinds, respectively, and $\rho_{ij}^0 = 2\sqrt{r_i r_j}/(r_i + r_j)$. Near the plate, amplitude and phase of the factor β specify current in the inner drive coil needed to null interference at the receiver.

3.0 FLAW SIGNAL DESCRIPTION

In order to examine response of a microprobe to a flaw, we first determine response of a single receiver loop to perturbation of eddy currents by a small void embedded in a half–space of uniform electrical conductivity σ. Electric current oscillating in a source coil, coplanar and concentric with the receiver loop, drives eddy currents in the conducting half space. Figure 3.1 shows the loops at height h above a half space. A flaw is at depth d and radial distance r_f from the center of the loops.

We first express the distribution of eddy currents excited by the source in a uniformly conducting half–space, then give the current perturbation produced by a flaw, and, finally, determine the response of the receiver loop to perturbed eddy currents.

3.1 INDUCED EDDY CURRENTS

Faraday's law in the form

$$\vec{\nabla} \times \vec{E} = -\partial \vec{B}/\partial t \tag{3.1a}$$

gives the electric field, $\vec{E}$, induced by a changing density of magnetic flux, $\vec{B}$, from an oscillating current. Ampere's law, expressed by the relation,

$$\vec{\nabla} \times \vec{H} = \vec{J} + \vec{J}_s \tag{3.1b}$$

relates magnetic field intensity, $\vec{H}$, to electric current density, $\vec{J}$, in the conducting region and current density, $\vec{J}_s$, of a source. Equations 3.1a and 3.1b together with Ohm's law, $\vec{J} = \sigma \vec{E}$, which relates current density to electric field, and the relation $\vec{B} = \mu_0 \vec{H}$, with $\mu_0 = 4\pi \times 10^{-7}$ H/m , which says that density of magnetic flux is proportional to magnetic field intensity, give current density and electric and magnetic fields above and within the conductor. Electric and magnetic fields parallel to the conductor boundary are continuous across the boundary.

To determine the fields, we express magnetic flux density as the curl of a vector potential, $\vec{A}$, so $\vec{B} = \nabla \times \vec{A}$ with $\nabla \cdot \vec{A} = 0$. Equations 3.1a and 3.1b then tell us that

$$\nabla^2 \vec{A} - \mu_0 \sigma \, \partial \vec{A}/\partial t = -\mu_0 \vec{J}_s \tag{3.2a}$$

with $\vec{E} = -\partial \vec{A}/\partial t$ and $\vec{J} = -\sigma \, \partial \vec{A}/\partial t$.

Appendix A derives the vector potential of an electric current oscillating at frequency ω in a circular loop of radius r_0 at height h above a conducting half–space. It shows that the relation

$$\vec{A}(r,z) = \vec{A}_0(r,z) + \frac{\mu_0 I r_0}{2} \hat{\phi} \int_0^\infty \left[\frac{1-\gamma/k}{1+\gamma/k}\right] e^{-k(z+h)} \, J_1(kr_0) \, J_1(kr) \, dk \, , \tag{3.2b}$$

gives the vector potential for $z > 0$, where

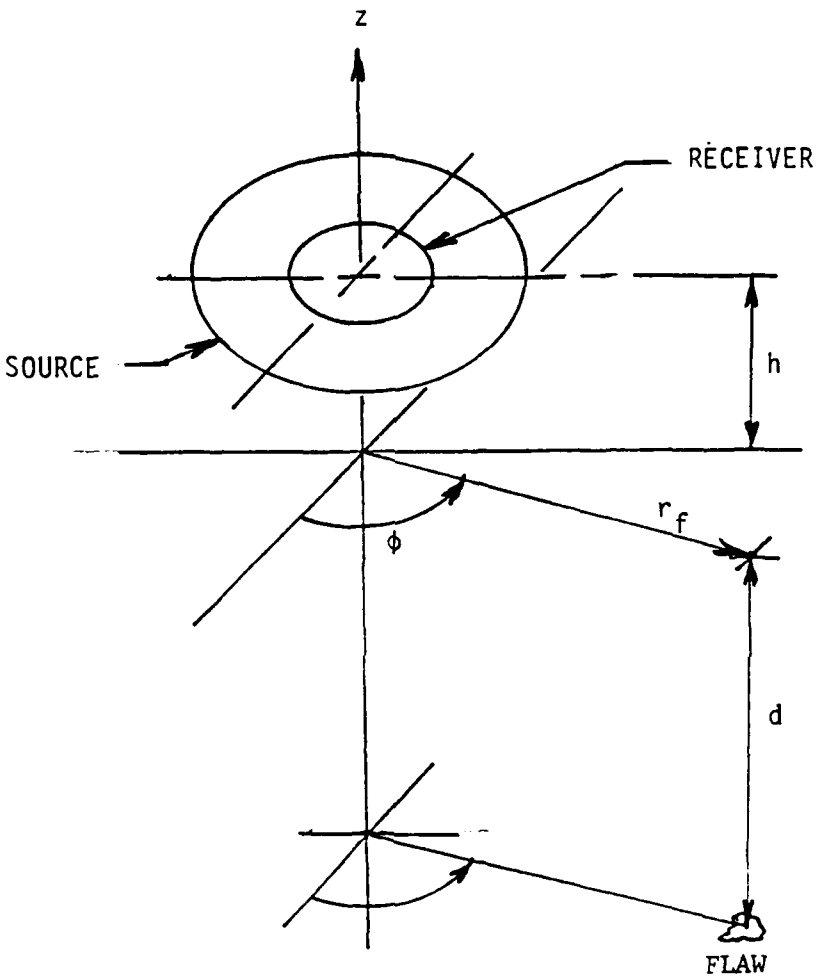

Figure 3.1

Coplanar source coil and receiver loop at height h above a half–space of uniform conductivtiy σ. A small void is at depth d and radius r_f from the center of the concentric loops. The origin of cylindrical coordinates r, ϕ, z is on the common axis of the loops at the surface of the half–space.

$$\vec{A}_o(r,z) = \frac{\mu_o I}{\pi\rho}\sqrt{\frac{r_o}{r}}\left[(1-\rho^2/2)\,K(\rho) - E(\rho)\right]\hat{\phi} \qquad (3.2c)$$

with $\rho^2 = 4rr_o/[(z-h)^2+(r_o+r)^2]$, is the vector potential of a current loop in free space (Smythe, 1969). The relation

$$\vec{A}(r,z) = \mu_o I r_o\,\hat{\phi}\int_0^\infty \left[\frac{e^{\gamma z - k h}}{\gamma/k + 1}\right] J_1(kr_o)\,J_1(kr)\,dk \qquad (3.2d)$$

gives it for $z < 0$. Here, $\gamma^2 = k^2 + i\mu_o\sigma\omega$ and $J_1(x)$ is a Bessel function of the first kind and order one. Because the source current is in the direction $\hat{\phi}$ of cylindrical coordinates r, ϕ, and z, so is its vector potential for a uniformly conducting half–space.

Electric field and current distributions are proportional to $\vec{A}(r,z)$; namely, $\vec{E}(r,z) = -i\omega\,\vec{A}(r,z)$ and $\vec{J}(r,z) = -i\omega\sigma\,\vec{A}(r,z)$, where Equations 3.2b and 3.2d express $\vec{A}(r,z)$. Appendix A gives expressions for the corresponding density of magnetic flux, $\vec{B}$.

3.2 EDDY CURRENT PERTURBATION

Eddy currents induced in a uniformly conducting half–space by a current oscillating in a circular loop above the surface flow in concentric circles about the axis of the source loop. Following Burrows, 1964, we take a flaw as a small, spherical void that perturbs the circular flow of eddy currents. For a flaw that is much smaller than a skin depth and that is far from boundaries, induced current is effectively uniform over its dimensions.

A spherical void imbedded in a uniform current flow diverts current around the sphere. The diverted flow is the sum of a uniform flow and flow from a current dipole at the center of the spherical void. The relation (Panofsky and Phillips, 1962)

$$\vec{m} = -(3/2)V\,\vec{J}_o \qquad (3.3a)$$

expresses the current dipole, $\vec{m}$, in terms of the incident, uniform current $\vec{J}_o$ and volume of the void, V . The flow outside a flaw is the sum $\vec{J}_o+\vec{J}_1$, where the expression

$$\vec{J}_1 = \frac{1}{4\pi r^5}\left[2(\vec{m}\cdot\vec{r})\vec{r} - \vec{r}\times(\vec{m}\times\vec{r})\right] \qquad (3.3b)$$

gives the dipole form of current scattered by a flaw, with $\vec{r}$ a radial vector measured from the center of the flaw.

Current inside a flaw vanishes, but the electric field within a flaw is $(3/2)\vec{E}_o$, where $\vec{E}_o = \vec{J}_o/\sigma$ and is the uniform electric field induced at a flaw. Total electric field outside a flaw is the sum $\vec{E}_o+\vec{E}_1$, where the electric field scattered by a flaw, $\vec{E}_1$, is $\vec{J}_1/\sigma$.

The dipole opposes the induced current in order to null electric current within a flaw. It arises from a uniform current density $-\vec{J}_0$ throughout the sphere that cancels the uniform current induced within the flaw. For either an irregular flaw volume or a nonuniform incident current, the diverted or scattered current outside a flaw comprises multipoles of higher order.

3.3 MAGNETIC FLUX PERTURBATION

To determine the perturbation in magnetic flux resulting from electric current diverted by a flaw, we again follow Burrows, 1964, and use a reciprocity theorem (Appendix C). The expression

$$\int \vec{A}_f \cdot \vec{J}_r \, d\mathcal{V} = \int \vec{A}_r \cdot \vec{J}_f \, d\mathcal{V} \tag{3.4}$$

states reciprocity in terms of vector potentials and impressed current densities. It says that the volume integral of the scalar product of a current density in a receiver loop, $\vec{J}_r$, with the vector potential from the current dipole of a flaw, $\vec{A}_f$, is equivalent to the volume integral of the scalar product of the current dipole of a flaw, $\vec{J}_f$, with the vector potential from current in the receiver loop, $\vec{A}_r$.

Because the receiver loop is a current filament, the volume integral containing the receiver current density is simply the product of current in the loop, I_r, and flux threading the loop, Φ_f, that results from the current dipole of the flaw; namely,

$$\int \vec{A}_f \cdot \vec{J}_r \, d\mathcal{V} = I_r \, \Phi_f \, . \tag{3.5a}$$

The vector potential *within* a flaw from current in the receiver loop, $\vec{A}_r$, is $(3/2)\vec{A}_r^o$, where $\vec{A}_r^o$ is the vector potential induced *at* the flaw from current in the receiver loop. Equation 3.3a gives current density in a flaw, $\vec{J}_f = -\vec{J}_0$, in terms of the current dipole, so the relation

$$\int \vec{A}_r \cdot \vec{J}_f \, d\mathcal{V} = \vec{A}_r^o \cdot \vec{m} \tag{3.5b}$$

expresses the volume integral in terms of the current dipole moment and the vector potential induced at the flaw by a current I_r in the receiver loop. Equations 3.4, 3.5a, and 3.5b then tell us that the expression

$$\Phi_f = \frac{\vec{m} \cdot \vec{A}_r^o}{I_r} \tag{3.5c}$$

gives the perturbed flux threading a receiver loop as a result of eddy currents diverted by a flaw.

3.4 ELEMENTAL FLAW SIGNAL

To determine the signal in a single receiver loop from a flaw illuminated by a single source coil, we combine Equation 3.3a, giving the current dipole that describes diversion of eddy currents, with Equation 3.5c, giving the flux threading a receiver loop from eddy currents diverted by a flaw. Namely, the expression

$$\vec{m} = (3/2)V\, i\omega\sigma\, \vec{A}_s \ , \tag{3.6a}$$

gives the current dipole in terms of the vector potential $\vec{A}_s$ produced at a flaw by a source current I_s oscillating at frequency ω, so Equation 3.5c tells us that the expression

$$\frac{\Phi_r}{I_s} = \frac{3}{2} V\, i\omega\sigma \left[\frac{\vec{A}_s \cdot \vec{A}_r^{\,o}}{I_s\ I_r}\right] \tag{3.6b}$$

gives flux threading the receiver loop, Φ_r, for unit current in the source coil, where $\vec{A}_r^{\,o}$ is the vector potential produced at the flaw by a current I_r in the receiver loop. Vector potentials take the form expressed by Equation 3.2d.

For a coplanar and concentric source coil and receiver loop at height h above a conducting half–space, we use Equation 3.2d to express Equation 3.6b in the form

$$F(r_f,d) = \mu_o \frac{3}{2} V\, i\mu_o\omega\sigma\, N_0 r_0\, N_1 r_1\, Y_0(r_f,d)\, Y_1(r_f,d) \tag{3.7a}$$

that gives the flux threading the receiver loop, $F(r_f,d)$, resulting from a flaw of volume V at depth d and radial distance r_f from the center of the loops, for a unit current in the source coil. The source coil comprises N_0 turns of radius r_0, and the receiver has N_1 turns of radius r_1. Here, the expression

$$Y_i(r,d) = \int_0^\infty \left[\frac{e^{-\gamma d - kh}}{\gamma/k + 1}\right] J_1(kr_i)\, J_1(kr)\, dk \tag{3.7b}$$

gives the distribution of eddy currents with depth, d, and radial distance, r, from a driving loop of radius r_i at height h. It measures sensitivity of the loops to a flaw at depth d and radial distance r.

4.0 MICROPROBE RESPONSE TO A FLAW

Equation 3.7a gives the elements of the signal from a flaw. It describes the response of a single receiver loop to a flaw illuminated by eddy currents driven by a single source coil. A microprobe comprises a source formed by two opposed coils and a receiver of n loops forming a gradiometer of order n. To describe its response to a flaw, we write the source and receiver factors of Equation 3.7a as sums of factors for multiple source coils and receiver loops of a microprobe. We number the two source coils 0 and 1 and number the n receiver loops from 2 through 2+n.

As Figure 1.1 shows, two coplanar source coils encircle n coplanar and concentric loops of the receiver that form a gradiometer of order n. Electric current I_1 oscillating in the inner source coil balances current I_0 oscillating in the outer coil in order to null interference from the source at the receiver. A balance factor β gives their complex ratio; namely, $I_1 = -\beta I_0$.

The expression

$$\vec{A}_s(r_f,d) = \mu_o I_0 \left[N_0 r_0 \, Y_0(r_f,d) - \beta N_1 r_1 \, Y_1(r_f,d) \right] \hat{\phi} \tag{4.1}$$

then gives the vector potential of the source at a flaw located at depth d and radial position r_f. Here, Equation 3.7b gives the distribution, $Y_i(r,d)$, of eddy currents with depth, d, and radial distance, r, from a driving loop of radius r_i at height h, and Equation 2.6a expresses the balance factor β in terms of mutual inductances between source coils and receiver loops. Amplitude and phase of the factor β specify current in the inner drive coil needed to make net flux from the source vanish in the receiver loops.

The expression

$$\left[\frac{\vec{A}_r^{\,o}}{I_r} \right]_n = \mu_o \hat{\phi} \sum_{i=2}^{n+2} N_i r_i \, Y_i(r_f,d) \tag{4.2}$$

gives the net vector potential at a flaw for unit currents in the n receiver loops. It tells sensitivity of a receiver of order n to flux perturbed by a flaw. Equation 2.2b specifies number of turns N_i and radii r_i of the n receiver loops that give a gradiometer of order n.

Equations 4.1 and 4.2 together with Equation 3.6b then tell us that the expression

$$G_n(r_f,d) = \mu_o \frac{3}{2} V \, i\mu_o \sigma \omega \, I_0 \left[N_0 r_0 \, Y_0(r_f,d) - \beta N_1 r_1 \, Y_1(r_f,d) \right] \sum_{i=2}^{n+2} N_i r_i \, Y_i(r_f,d) \tag{4.3}$$

gives the response of a microprobe, $G_n(r_f,d)$, with a receiver forming a gradiometer of order n, to a spherical flaw of volume V at depth d and radial position r_f from the center of the microprobe. The response is the net flux threading the receiver for a current I_0 in the outermost coil of two balanced source coils.

We describe the response for microprobes of order two and four. A gradiometer of odd order gives the same response as the preceding one of even order, because the response to a dipole contains even powers of r alone. The microprobe carries a current I_0 in the main drive coil, oscillating at frequency f , and sits at height h above a thick aluminum plate, with $\sigma = 3.54 \times 10^7$ mhos/m . A spherical flaw 0.1 mm in radius is at depth d in the plate and at radial distance r_f from the center of the microprobe. In each case, we give the net flux threading the receiver in units of a flux quantum, ϕ_0 , for a current of one ampere in the source; namely, $\Gamma_n = G_n/\phi_0/I_0$, where Equation 4.3 gives the net flux, G_n , threading the receiver. A flux quantum is 2.07×10^{-15} Tm^2 .

4.1 RESPONSE OF A SECOND ORDER MICROPROBE

We give the response of a microprobe, with a receiver formed by a gradiometer of second order, to a spherical flaw 0.1 mm in radius in an aluminum plate using values listed in Table 4.1 for number of turns and radii, in millimeters, of source coils and receiver pickup loops. Source coils are numbers 0 and 1 ; receiver loops are numbers 2 and 3 .

TABLE 4.1

COIL SPECIFICATIONS FOR A MICROPROBE OF SECOND ORDER

i	0	1	2	3
N_i	16	–4	1	–4
r_i , mm	3	2	1	0.5

Figure 4.1 shows magnitude of the complex response of a microprobe of second order, as a function of radial distance, to a 0.1 mm flaw at fixed depths spaced 0.5 mm apart, ranging from 0.5 mm to 5 mm. The microprobe carries a current of one ampere in the main drive coil, oscillating at a frequency of 1 kHz, and sits 1 mm above the surface. Skin depth in aluminum is 2.68 mm at a frequency of 1 kHz.

The response shows a peak near a radius of 1 mm that migrates to larger radii as flaw depth increases. Peak magnitude decreases markedly at radial distances and/or flaw depths greater than a skin depth, but still exceeds SQUID sensitivity of 10^{-4} $\phi_0/\sqrt{\text{Hz}}$ out to about 13 mm in radius and 8 mm in depth, as shown in the next figure.

Figure 4.2 shows contours of constant magnitude in the r,z plane for flaw depths to 8 mm and radii out to 14 mm. Contours range from a magnitude of 10 ϕ_0/A to 10^{-4} ϕ_0/A . Contours show that peak response exceeds SQUID sensitivity out to radii of 13 mm or so and depths to 8 mm, for a drive current of 1 A. The line cutting across contours traces migration of peak response with flaw depth. It gives a measure of horizontal resolution of a microprobe, as section 5.4 shows.

Figure 4.3 shows magnitude at the peak as a function of drive frequency, for flaw depths of 1 mm, 3 mm, 5 mm, 7 mm, and 10 mm. It shows that peak response increases linearly with drive frequency, reaches a broad maximum, and then decreases sharply. Because amplitudes of eddy currents increase in proportion to frequency, response increases linearly with frequency until losses in the conductor dominate and then decrease sharply, as skin depth decreases with increasing frequency. For internal flaws at depths exceeding 1 mm, operating at a several hundred to a few thousand Hertz is best. For flaws near the surface, frequencies of several thousand Hertz are best.

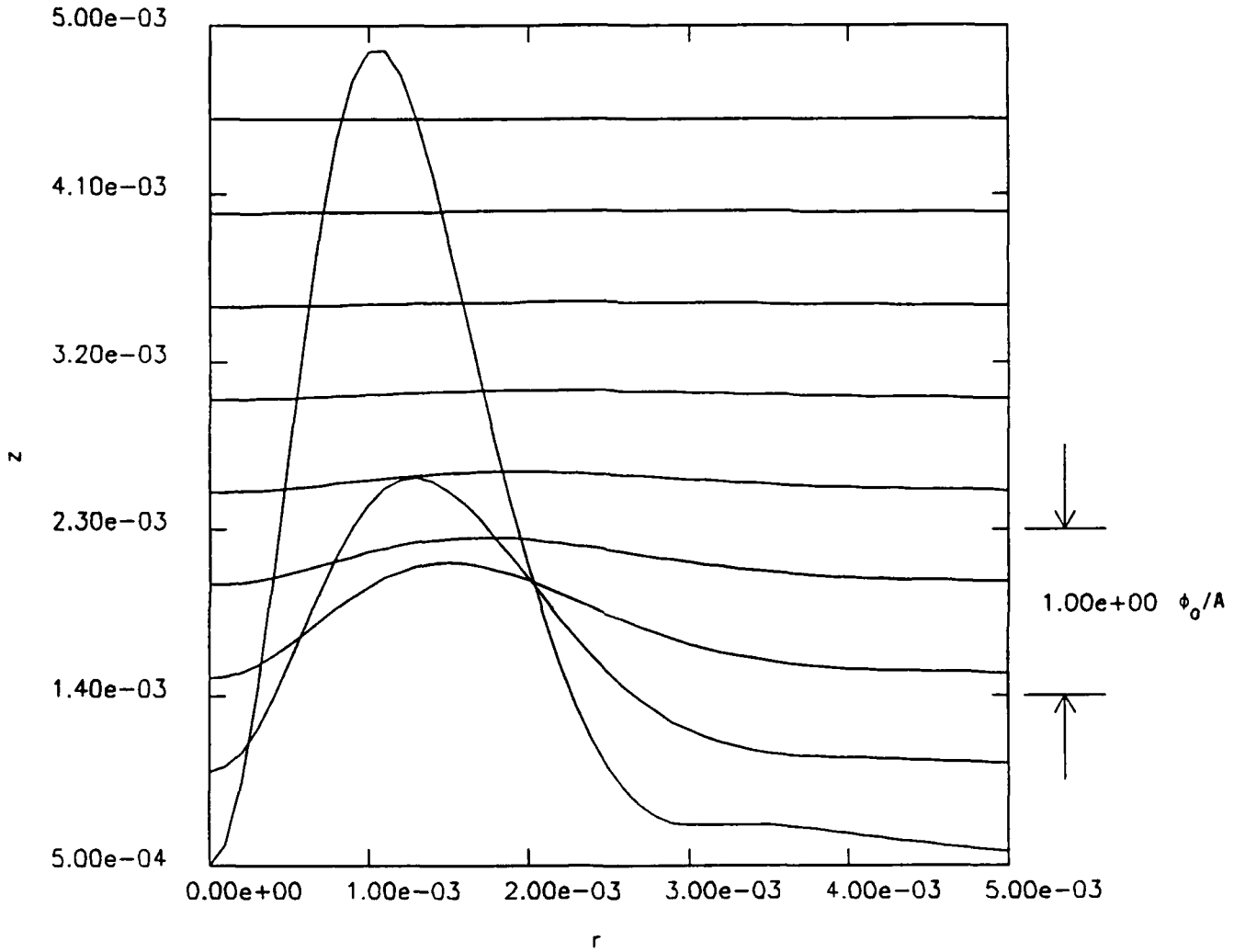

Figure 4.1

Magnitude of the complex response of a microprobe of second order, shown as a function of radial distance, to a 0.1 mm flaw at fixed depths spaced 0.5 mm apart, ranging from 0.5 mm to 5 mm. The microprobe carries a current of one ampere in the main drive coil, oscillating at a frequency of 1 kHz, and sits 1 mm above the surface. Abscissa measures radial distance in millimeters, and the left hand ordinate measures depth in millimeters. Right hand ordinate measures gain of the response in ϕ_o/A . Peak response for a 0.1 mm flaw at a depth of 0.5 mm is 4.84 ϕ_o/A.

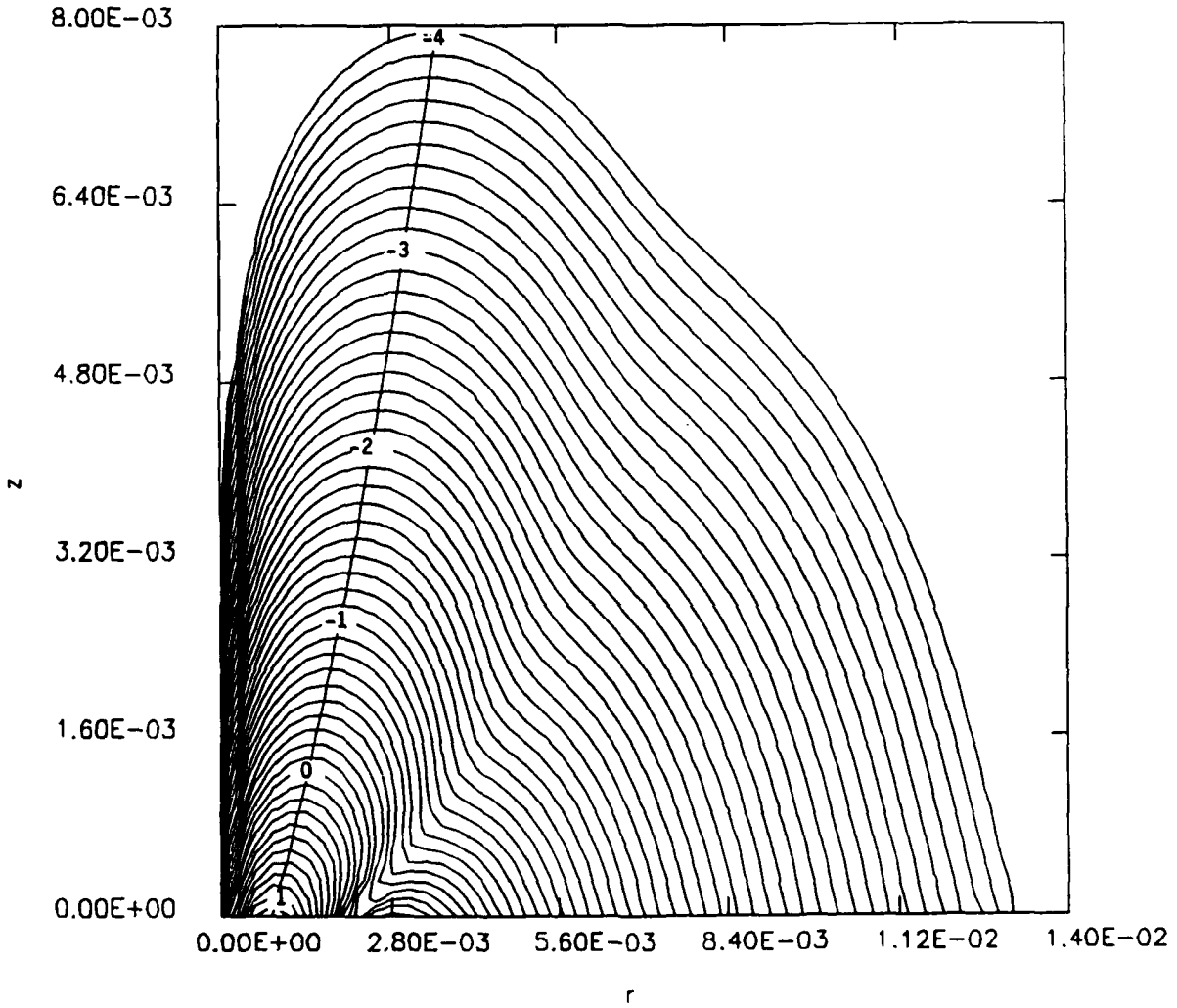

Figure 4.2

Contours of constant magnitude in the r,z plane for flaw depths, z, from zero to 8 mm and radii, r, from zero to 14 mm. Contours range from a magnitude of $10\ \phi_o/A$ to $10^{-4}\ \phi_o/A$, spaced logarithmically at intervals of 0.1 in the exponent. The line cutting across contours traces the locus of peak magnitude. Tick marks on the locus mark contours at decades from $10\ \phi_o/A$ to $10^{-4}\ \phi_o/A$.

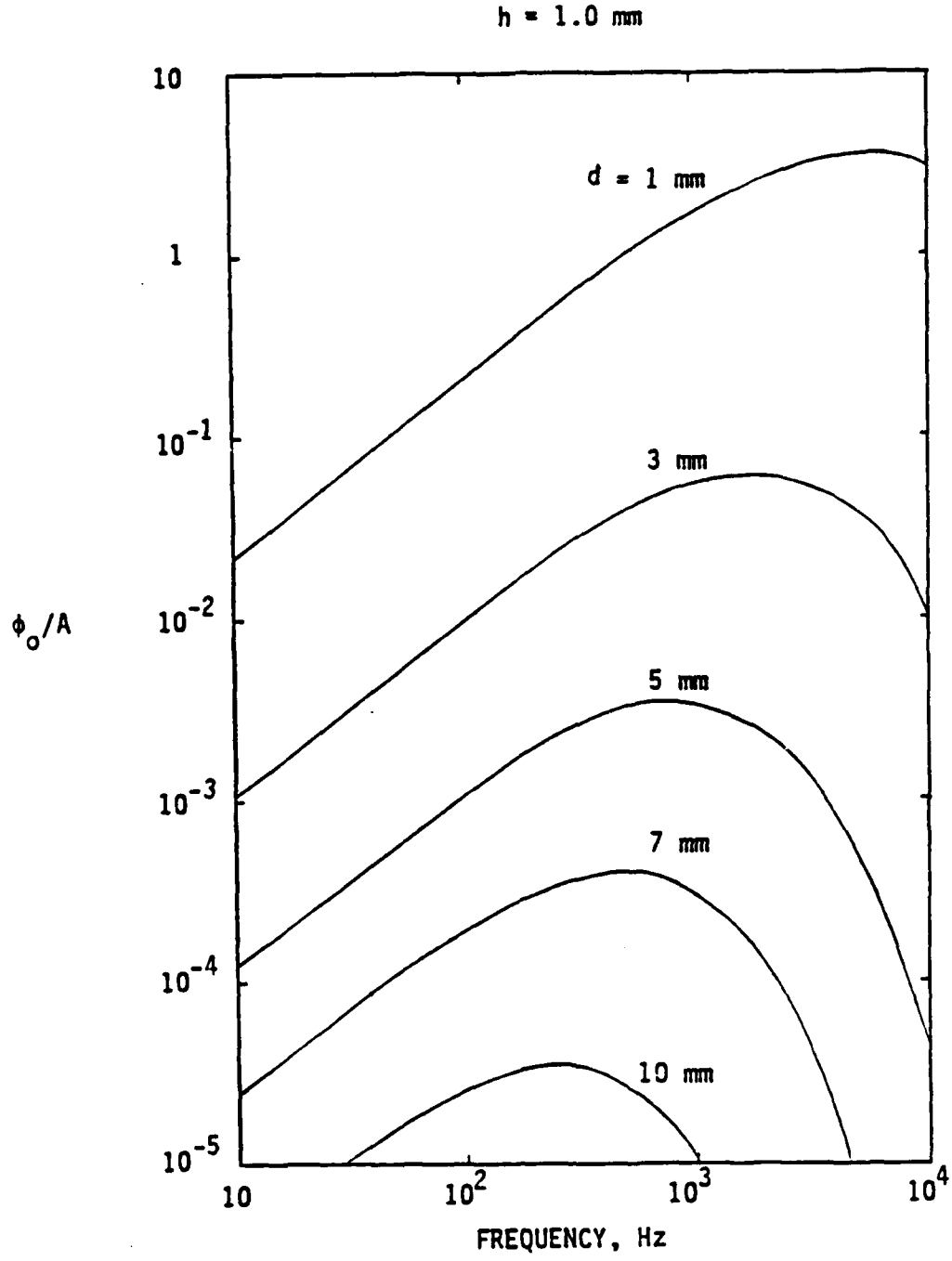

Figure 4.3

Peak response of a microprobe of second order shown as a function of frequency for a spherical flaw 0.1 mm in radius at depths, d , of 1 mm, 3 mm, 5 mm, 7 mm, and 10 mm in a thick aluminum plate. Height of the microprobe above the surface, h , is 1 mm. The ordinate axis measures response in flux quanta, ϕ_o , for a current of one ampere oscillating in the outermost drive coil at frequencies ranging from ten Hertz to ten thousand Hertz, as marked on the abscissa.

4.2 RESPONSE OF A FOURTH ORDER MICROPROBE

We describe response of a microprobe, with a receiver formed by a gradiometer of fourth order, to a spherical flaw 0.1 mm in radius in an aluminum plate using values listed in Table 4.2 for number of turns and radii, in millimeters, of source coils and receiver pickup loops. Source coils are numbers 0 and 1 ; receiver loops are numbers 2, 3, 4, and 5 .

TABLE 4.2

COIL SPECIFICATIONS FOR A MICROPROBE OF FOURTH ORDER

i	0	1	2	3	4	5
N_i	16	–4	1	–2	2	–2
r_i , mm	3	2	1	0.90	0.64	0.31

Figure 4.4 shows magnitude of the complex response of a microprobe of fourth order, as a function of radial distance, to a 0.1 mm flaw at fixed depths spaced 0.5 mm apart, ranging from 0.5 mm to 3 mm. The microprobe again carries a current of one ampere in the main drive coil, oscillating at a frequency of 1 kHz, and sits 1 mm above the surface.

The response shows a primary peak near a radius of 0.6 mm and a secondary peak near a radius of 1.8 mm. Peaks migrate to larger radii as flaw depth increases. The two peaks form two lobes on contours shown in the following figure.

Figure 4.5 shows contours of constant magnitude in the r,z plane for flaw depths to 4 mm and radii out to 5 mm. Contours range from a magnitude of 0.5 ϕ_o/A to 10^{-4} ϕ_o/A . Contours show that peak response exceeds SQUID sensitivity out to radii of about 5 mm and depths to 3.5 mm, for a drive current of 1 A. The line cutting across contours traces migration of peak response with flaw depth. It gives a measure of horizontal resolution of a microprobe, as section 5.4 shows.

Figure 4.6 shows magnitude of the primary peak as a function of drive frequency, for flaw depths of 0.5 mm, 1 mm, 2 mm, and 3 mm. Peak response again increases linearly with drive frequency, reaches a broad maximum, and then decreases sharply as losses in the conductor dominate. For internal flaws at depths exceeding 1 mm, operating at a few hundred to a thousand Hertz is best. For flaws near the surface, frequencies of several thousand Hertz are best.

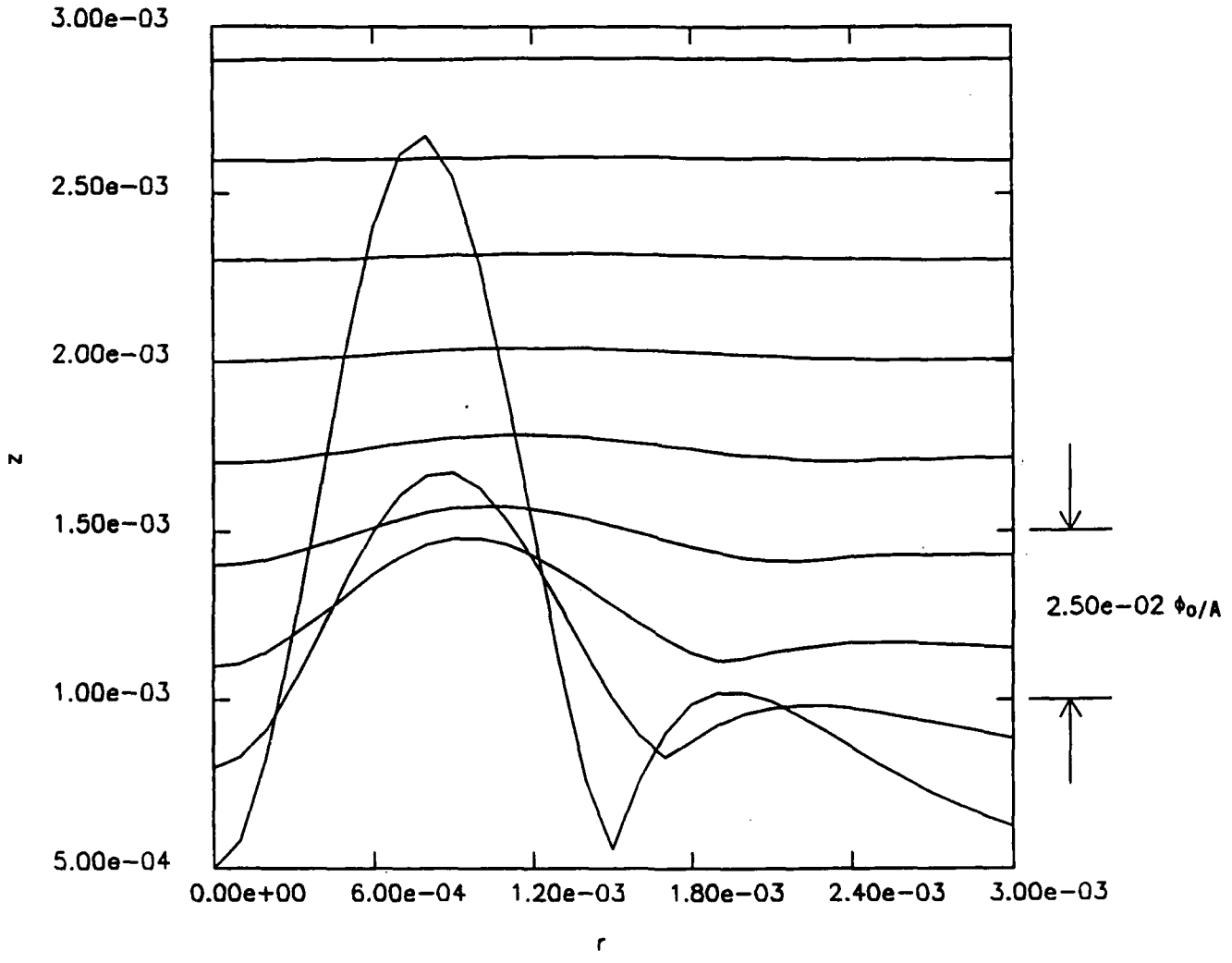

Figure 4.4

Magnitude of the complex response of a microprobe of fourth order, shown as a function of radial distance, to a 0.1 mm flaw at fixed depths spaced 0.3 mm apart, ranging from 0.5 mm to 3 mm. The microprobe carries a current of one ampere in the main drive coil, oscillating at a frequency of 1 kHz, and sits 1 mm above the surface. Abscissa measures radial distance in millimeters, and the left hand ordinate measures depth in millimeters. Right hand ordinate shows gain of the response, which is 0.025 ϕ_o/A per division. Peak response for a 0.1 mm flaw at a depth of 0.5 mm is 0.108 ϕ_o/A.

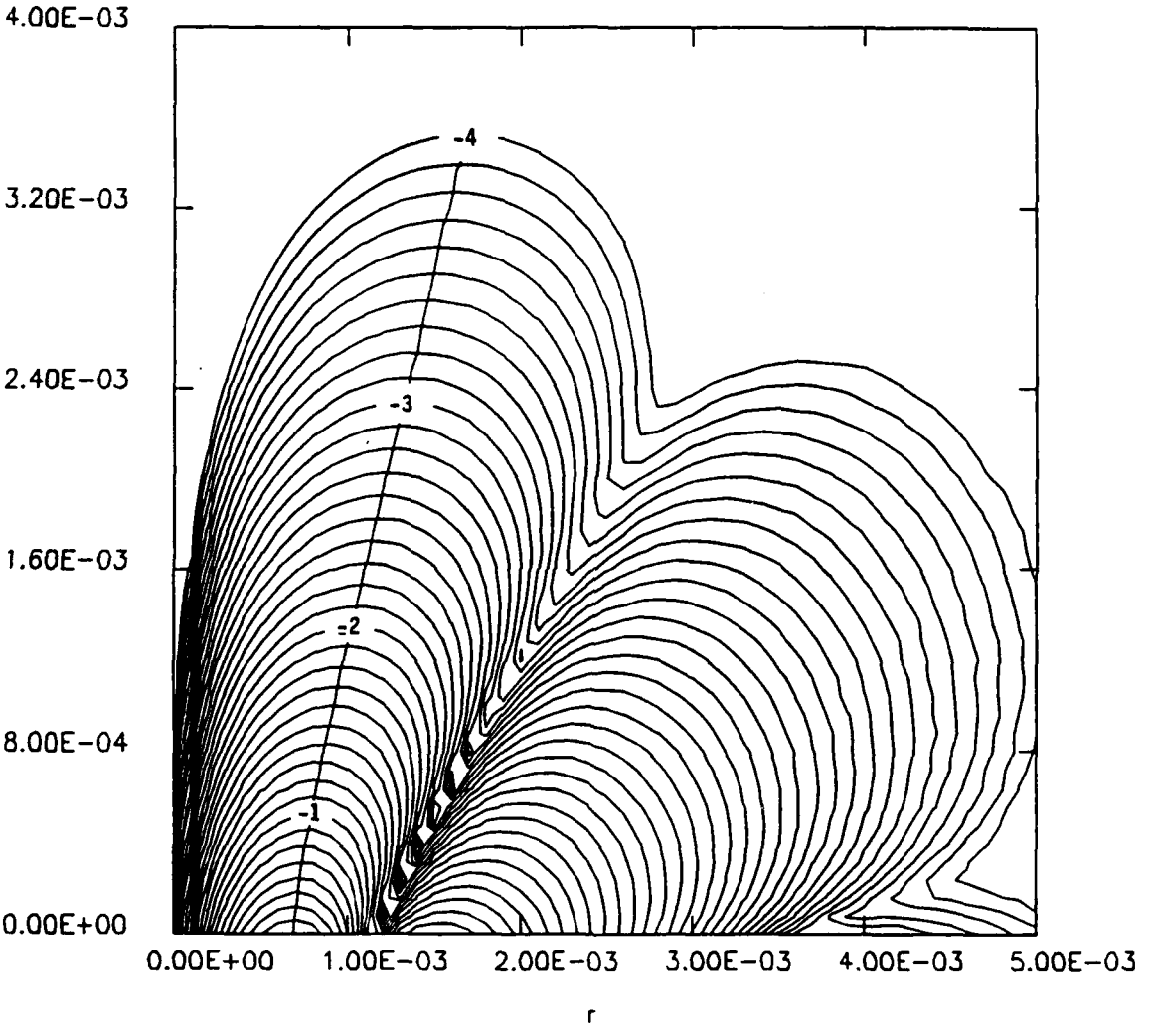

Figure 4.5

Contours of constant magnitude in the r,z plane for flaw depths, z, to 4 mm and radii, r, to 5 mm. Contours range from a magnitude of 0.468 ϕ_o/A to 10^{-4} ϕ_o/A, spaced logarithmically at intervals of 0.1 in the exponent. The line cutting across contours traces the locus of peak magnitude. Tick marks on the locus mark contours in decades from 10^{-1} ϕ_o/A to 10^{-4} ϕ_o/A.

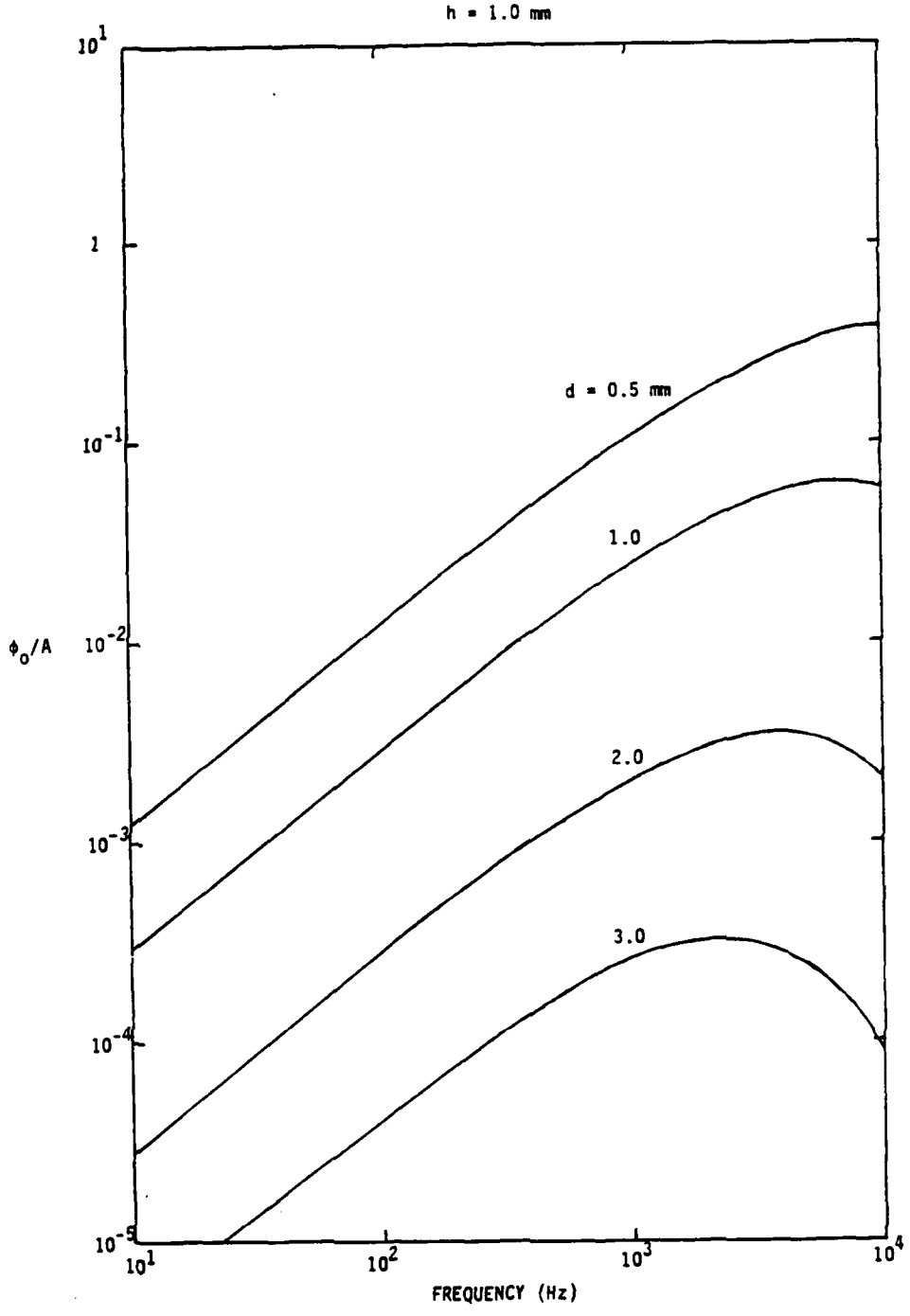

Figure 4.6

Peak response of a microprobe of fourth order shown as a function of frequency for a spherical flaw 0.1 mm in radius at depths, d , of 0.5 mm, 1 mm, 2 mm, and 3 mm in a thick aluminum plate. Height of the microprobe above the surface, h , is 1 mm. The ordinate axis measures response in flux quanta, ϕ_o , for a current of one ampere oscillating in the outermost drive coil at frequencies ranging from ten Hertz to ten thousand Hertz, as marked on the abscissa.

5.0 ELECTROMAGNETIC MICROSCOPE

High sensitivity of a superconductive microprobe provides high resolution needed to image internal flaws in aluminum. To form images, we cluster microprobes to form an array much like rods in the retina of a magnetic eye. The eye enables high scan rates at high resolution needed to develop an electromagnetic microscope for nondestructive evaluation of materials.

Here, we set forth the concept of an array of microprobes forming a magnetic eye and examine its depth of field, field of view, and resolution.

5.1 ELEMENTS OF A MAGNETIC EYE

An array of microprobes forming the eye of an electromagnetic microscope comprises pairs of parallel rows. Figure 5.1 shows a segment of one pair comprising biaxial microprobes of second order. Spacing between centers of microprobes in each row is four times the radial field of view. Offset and spacing between rows is set so microprobes form a pattern of equilateral triangles, with their centers separated by four times the radial field of view. It is both the smallest spacing without overlap and the widest spacing that gives complete coverage.

Closest packing of microprobes at a separation of twice the field of view gives double coverage for two parallel rows or complete coverage for a single row. Nonetheless, closest packing gives highest interference between probes. Effectiveness of the interior source coils of each probe in nulling interference determines minimum allowed array spacing. Because of symmetry, null settings of currents are equal in each microprobe, so they connect in series.

Because field of view changes with flaw depth and operating frequency, spacing of a pair of rows, or a single row, is set for greatest sensitivity at a specified depth range and operating frequency. A number of pairs comprises an eye, each with a spacing set for flaws at a specified depth. Pairs set to scan shallow flaws use a fourth order gradiometer in order to obtain high resolution. High resolution of a gradiometer of fourth order limits depth of field, so pairs set to scan flaws at depths of a several millimeters use gradiometers of second order. The receiver of each microprobe forms a biaxial gradiometer in order to give angular resolution.

5.2 DEPTH OF FIELD

We take depth of field as the depth at which the peak signal from a flaw falls below $10^{-4}\ \phi_0/\sqrt{\text{Hz}}$, which is the sensitivity of a SQUID sensor. Depth of field depends on flaw size, gradiometer order, and frequency and amplitude of the illuminating source current.

Figures 4.2 and 4.5 show contours of signal amplitude for gradiometers of second and fourth order, respectively. Contours tell depth of field to a flaw 0.1 mm in radius at an operating frequency of 1 kHz with a source current of 1 A. They show that depth of field is about 8 mm , for a gradiometer of second order, and is about 3.5 mm , for a gradiometer of fourth order. A second order gradiometer gives somewhat more than a twofold advantage in depth of field.

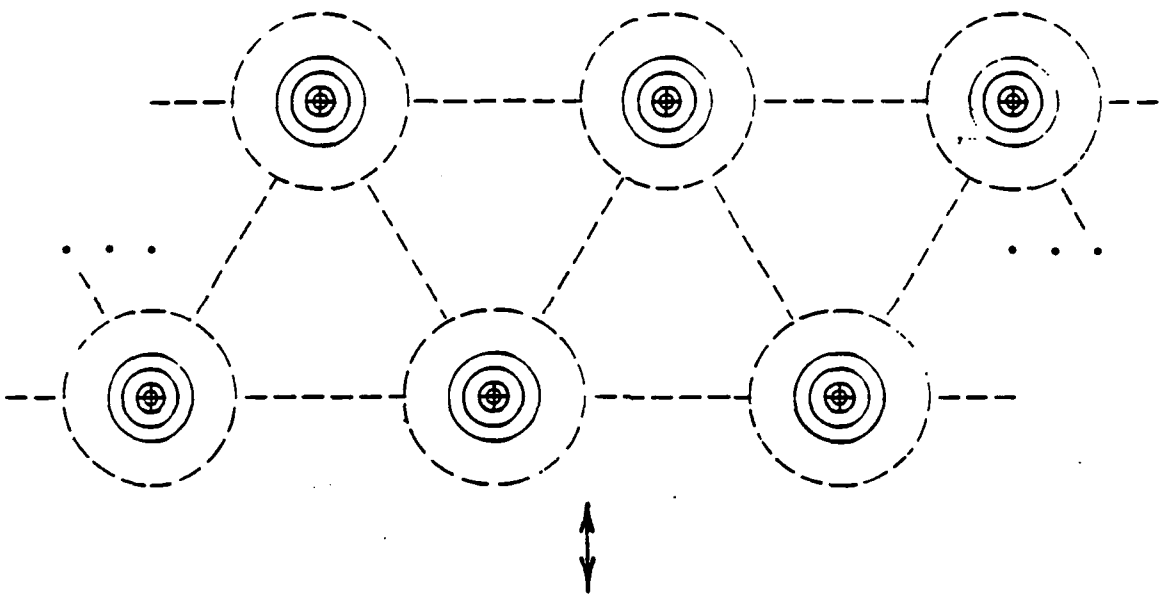

Figure 5.1

Segment of a pair of parallel rows of an array of biaxial microprobes forming a section of the eye of an electromagnetic microscope. Dashed circles mark the radial field of view for each microprobe. Dashed lines connecting their centers highlight the equilateral, triangular pattern, with a spacing between centers of four times the radial field of view. The arrow marks the direction of scan, and dots denote continuing replication of the array.

Figures 4.3 and 4.6 give peak signal amplitude as a function of operating frequency for flaws at fixed depths, for gradiometers of second and fourth order respectively. They show that drive frequencies of a few kilohertz give greatest signal amplitudes for flaw depths of a few millimeters. Depth of field, then, is greatest at frequencies of a few kilohertz and changes little with frequency at frequencies around 1 kHz.

Because signal amplitude is proportional to volume of a flaw, depth of field increases as the cube of flaw size. It also increases linearly with amplitude of the drive current, provided interference from the source remains null.

5.3 FIELD OF VIEW

We take field of view as the maximum radius at which the signal from a flaw falls below $10^{-4}\ \phi_0/\sqrt{\text{Hz}}$, for a flaw at a fixed depth. It depends on flaw size, gradiometer order, and frequency and amplitude of the drive current, as does depth of field.

Contours at $10^{-4}\ \phi_0/\text{A}$ in Figures 4.2 and 4.5 trace field of view as a function of flaw depth, for second and fourth order gradiometers, respectively, operating at a frequency of 1 kHz with a drive current of 1 A. Flaw size is again 0.1 mm. They show that field of view varies widely with depth of a flaw.

For a gradiometer of second order, field of view is about 3 mm for a flaw at the depth of field of about 8 mm. It increases to nearly 13 m for flaws near the surface. For a gradiometer of fourth order, field of view is about 1.5 mm for a flaw at the depth of field of about 3.4 mm. At greater depths, field of view vanishes. At shallower depths, it increases over the first lobe of the contour to about 3 mm at a depth of about 2.4 mm. Over the second lobe, it increases to a maximum value of about 5 mm at a depth of about 1 mm.

5.4 RESOLUTION

Contours of constant signal amplitude in a horizontal plane above a flaw are circles centered on the flaw. They give an image of a flaw that results from repeated scans over a flaw of a single microprobe or a single scan of a magnetic eye.

Figure 5.2a and Figure 5.2b show them at a height of 1 mm for a 0.1 mm flaw at a depth of 1.44 mm and 4.96 mm, respectively, for a gradiometer of second order with a drive current of 1 A oscillating at 1 kHz.

Figure 5.3a and Figure 5.3b show them for a gradiometer of fourth order at depths of 0.96 mm and 3.04 mm, respectively, again at a height of 1 mm for a 0.1 mm flaw with a drive current of 1 A oscillating at 1 kHz.

An eye gives multiple images, one for each row or pair of rows. They depend on gradiometer order and microprobe spacing in a row as well as frequency and amplitude of the drive current of a row. Multiple images can localize depth of a flaw. Gradiometers of fourth or higher order identify shallow flaws, and gradiometers of second order see deep as well as shallow flaws. For shallow flaws, ratios of image amplitudes from gradiometers of second and fourth order, for example, are independent of flaw size and depend on flaw depth alone, for fixed frequency and amplitude of drive currents. The information gives means of locating depth of a flaw. Alternatively, changing drive current and or frequency of a row moves its depth of field to the of depth of a flaw and so determines its depth. Using a pulsed waveform can also give flaw depth from the time delay of the scattered field.

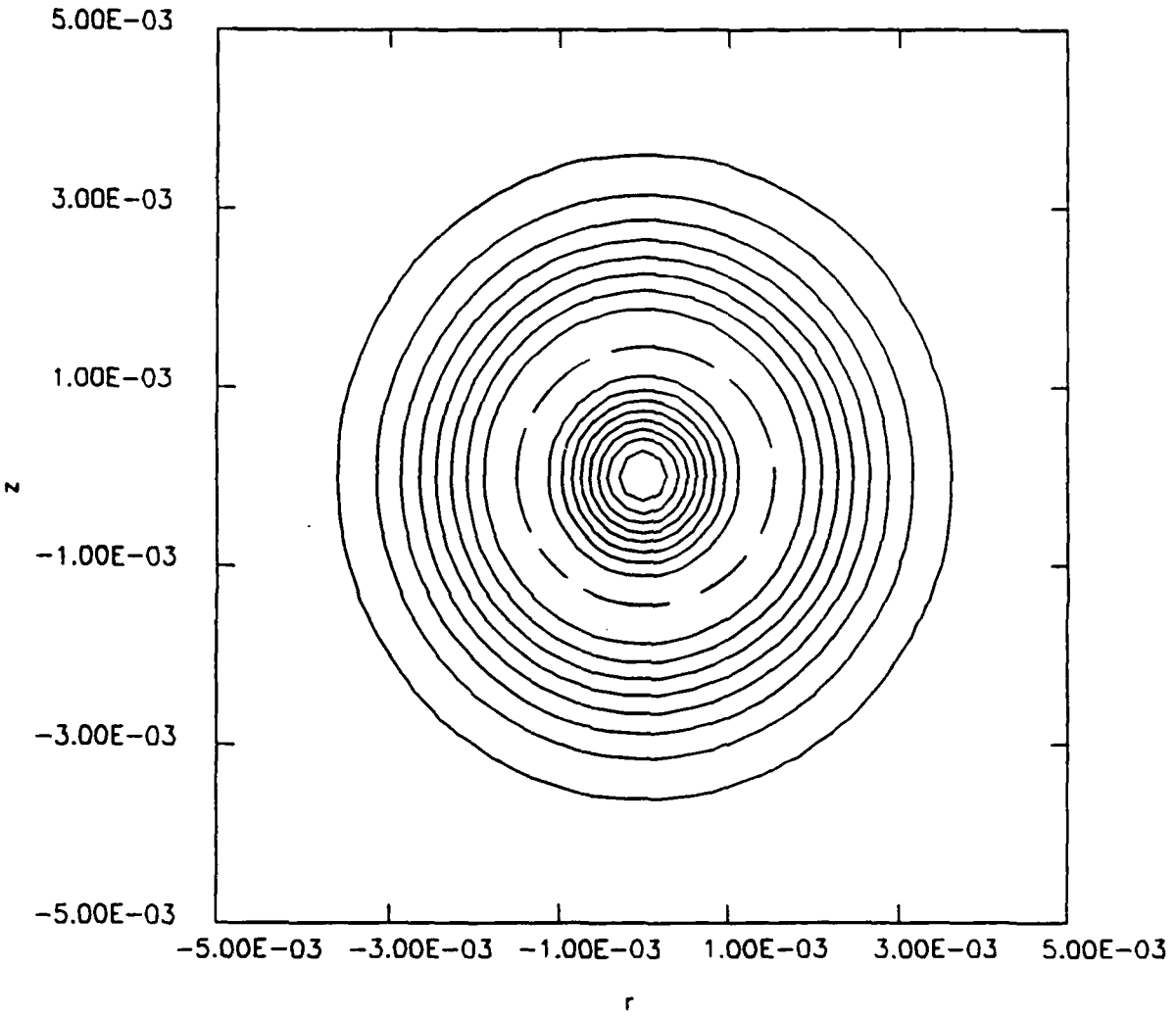

Figure 5.2a

Contours of constant signal amplitude in a horizontal plane at a height of 1 mm for a 0.1 mm flaw at a depth of 1.44 mm for a gradiometer of second order operating with a drive current of 1 A oscillating at 1 kHz. The dashed circle marks the peak signal amplitude. It gives a measure of horizontal resolution.

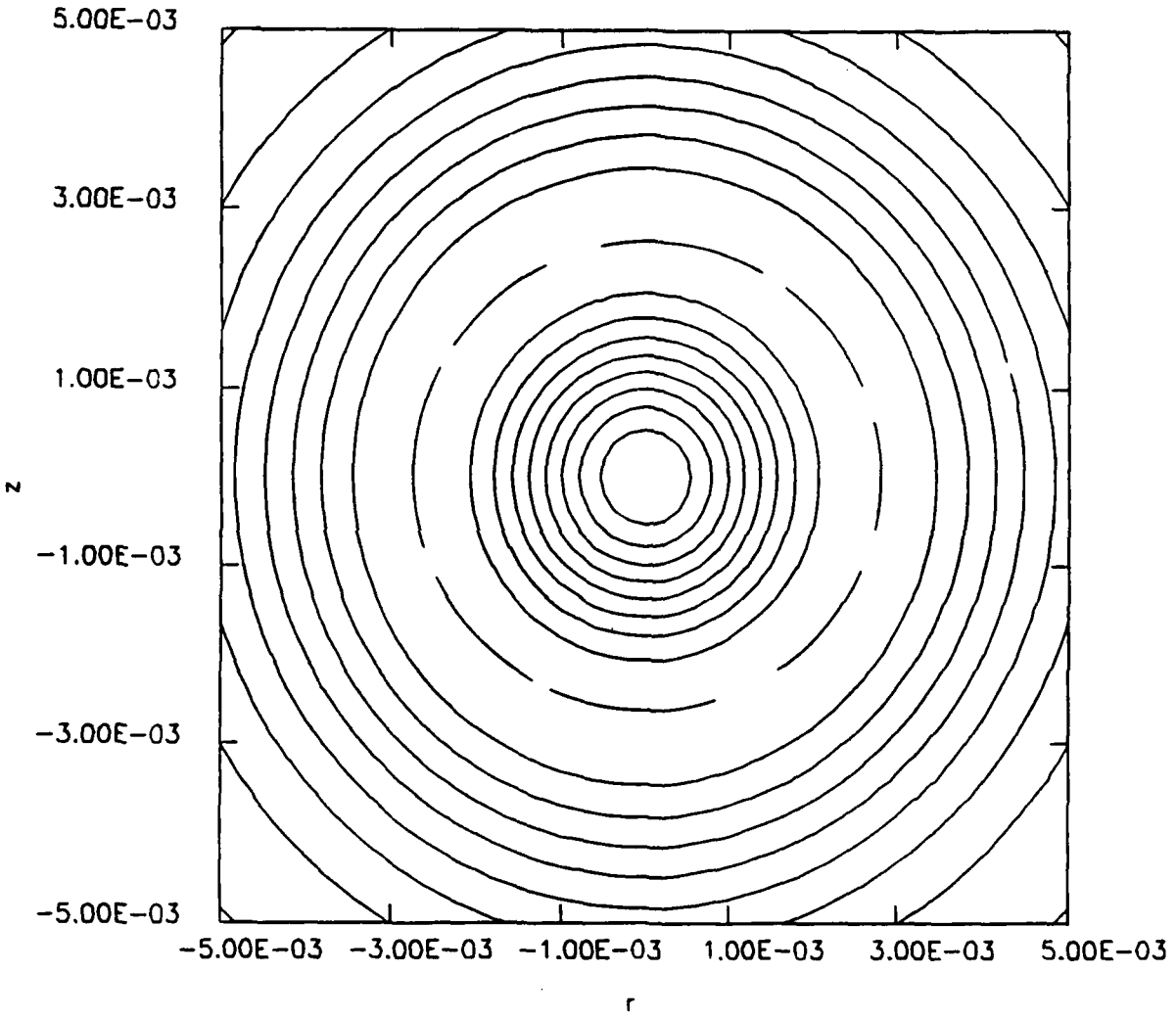

Figure 5.2b

Contours of constant signal amplitude in a horizontal plane at a height of 1 mm for a 0.1 mm flaw at a depth of 4.96 mm for a gradiometer of second order operating with a drive current of 1 A oscillating at 1 kHz. The dashed circle marks the peak signal amplitude. It gives a measure of horizontal resolution.

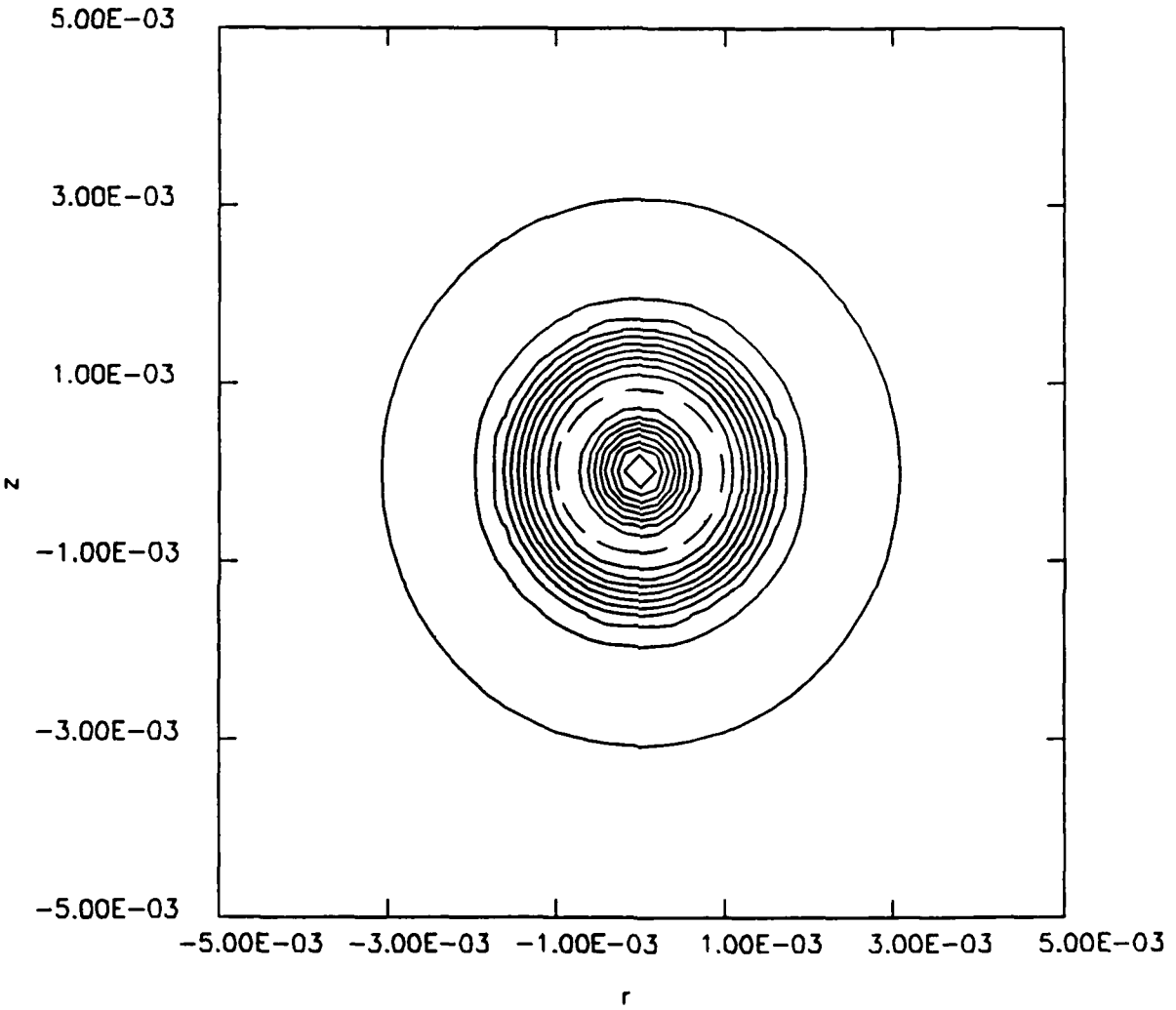

Figure 5.3a

Contours of constant signal amplitude in a horizontal plane at a height of 1 mm for a 0.1 mm flaw at a depth of 0.96 mm for a gradiometer of fourth order operating with a drive current of 1 A oscillating at 1 kHz. The dashed circle marks the peak signal amplitude. It gives a measure of horizontal resolution.

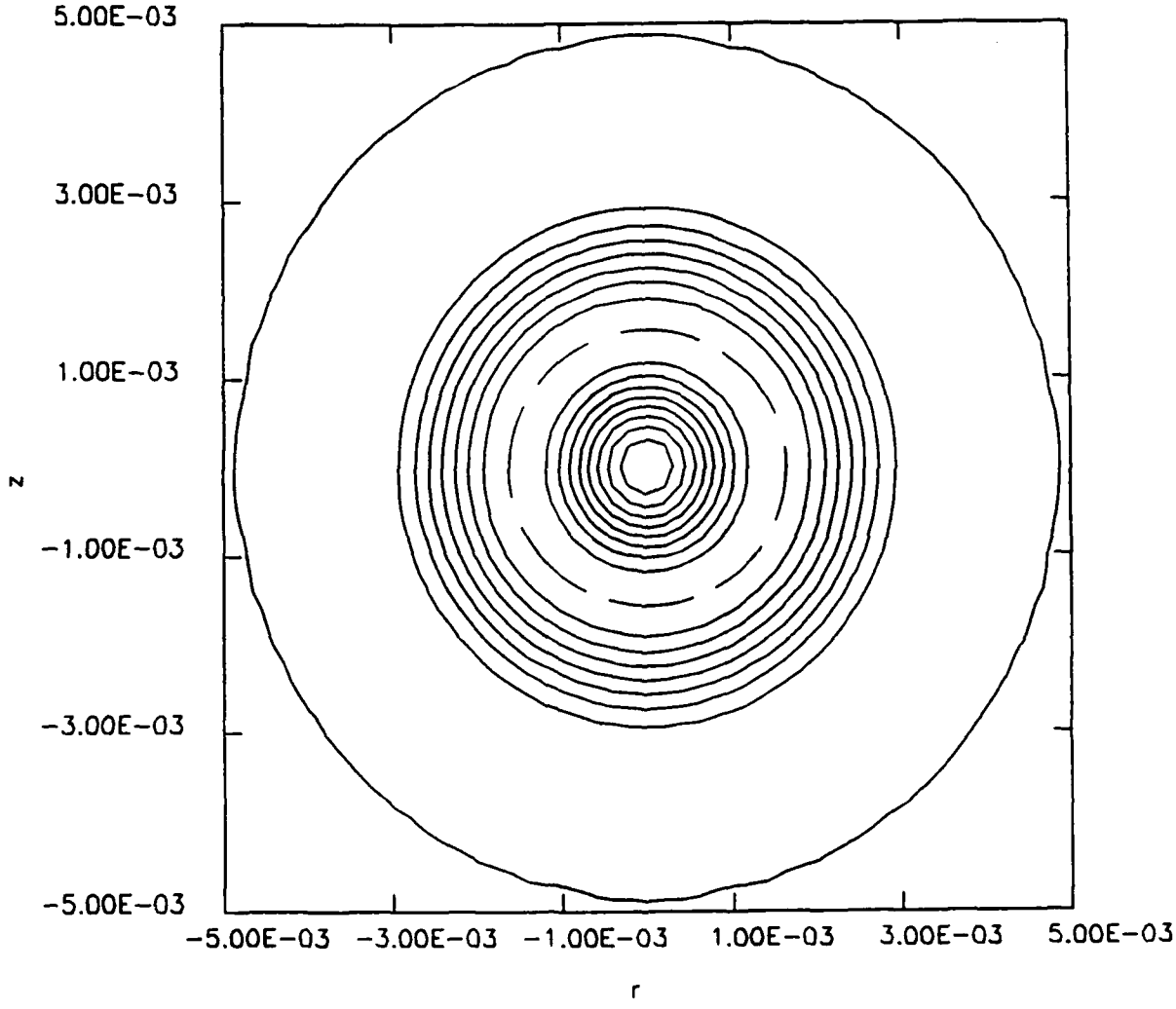

Figure 5.3b

Contours of constant signal amplitude in a horizontal plane at a height of 1 mm for a 0.1 mm flaw at a depth of 3.04 mm for a gradiometer of fourth order operating with a drive current of 1 A oscillating at 1 kHz. The dashed circle marks the peak signal amplitude. It gives a measure of horizontal resolution.

Radius of the contour marking the peak signal, highlighted by dashed circles in Figures 5.2a, 5.2b, 5.3a, and 5.3b, gives a measure of horizontal resolution for a magnetic eye. Radius increases, so resolution decreases, linearly with depth of a flaw. Figures 5.2a and 5.2b show the decrease in resolution from a flaw depth of 1.44 mm to 4.96 mm, for a gradiometer of second order. Figures 5.3a and 5.3b show it from 0.96 mm to 3.04 mm, for a gradiometer of fourth order.

The locus of peak signal in Figures 4.2 and 4.5 gives the linear change in resolution with flaw depth, for gradiometers of second and fourth orders respectively. For second order, we find that the relation

$$r_p = 0.371\ d + 0.792\ , \text{millimeters}, \tag{5.1a}$$

gives the radius of the contour marking the peak signal, r_p , for a flaw depth d , both measured in millimeters. Radius increases linearly from 0.792 mm for a surface flaw to 3.76 mm at the depth of field 8 mm. For fourth order, the relation

$$r_p = 0.256\ d + 0.65\ , \text{millimeters}, \tag{5.1b}$$

gives the contour radius. It increases linearly from 0.65 mm for a surface flaw to 1.55 mm at the depth of field of 3.52 mm.

Spacing of contours Figures 4.2 and 4.5 give a measure of vertical resolution for gradiometers of second and fourth orders respectively. Differences between contours represent a 26 % change in drive current amplitude. Near the depth of field, a 26 % change in current amplitude gives a change in depth of field of 0.24 mm for a second order gradiometer and 0.133 mm for a fourth order gradiometer. We expect, then, a vertical resolution of a few tenths of a millimeter for a 0.1 mm flaw.

6.0 ASSESSMENT OF FEASIBILITY AND TECHNICAL RISK

Successful development of an electromagnetic microscope for eddy current testing requires developing a microprobe, forming a magnetic eye from an array of microprobes, and demonstrating that performance of the eye surpasses that of conventional eddy current probes. Here we examine feasibility of the design of a microprobe and of a magnetic eye, identify main problems facing development, and estimate technical risk of developing an electromagnetic microscope.

6.1 FEASIBILITY

Analyses presented herein show that design of a high performance microprobe is feasible. A current of 1 A oscillating at a few kilohertz in a drive coil 3 mm in radius excites large enough eddy currents in an aluminum plate to give an appreciable signal in pickup loops 1 mm in radius from a 0.1 mm flaw at a depth of a few millimeters. Peak signal amplitude is several flux quanta, for a second order microprobe, and a few tenths of a flux quantum, for a fourth order microprobe. Peak amplitudes far exceed the probe sensitivity of $10^{-4}\ \phi_0/\sqrt{\text{Hz}}$. Loop sizes are well within the art of miniature fabrication techniques, and current densities required are modest for superconductive wire.

Although analyses demonstrate feasibility of the configuration and loop sizes of a microprobe, they allow performance to increase indefinitely with drive current. In practice, interference from the source coils sets the maximum allowable drive current and so limits performance. Nulling interference from the source is the central problem facing development of a microprobe as well as an array forming a magnetic eye.

Its solution comprises two main parts. First is to control current in the compensating drive coil in order to suppress interference in the pickup loops. Second is to apply an external feedback signal to the SQUID sensor in order to null residual interference. Interference from one ampere in the main drive coil, 3 mm in radius, is of the order of 10^7 flux quanta without compensation. External feedback to a SQUID sensor can compensate residual interference of a hundred flux quanta or so. Cuirrent in the compensating coil, then, must suppress interference by a factor of 10^4 to 10^5 in order to reduce it below 100 flux quanta. A circuit using a phase-locked oscillator to control amplitude and phase of current in the compensating coil within a few ppm of set values is within the art, so suppression by as much as a factor of 10^6 is practical. An overall, combined suppression by a factor of 10^8, then, is within the art, so drive currents of 1 to 10 amperes in a drive coil 3 mm in radius are feasible.

Compensation of a symmetric array of microprobes follows from that of a single microprobe. Symmetry of an array says that compensation for each microprobe is the same, so they connect in series. Drive coil compensation for a symmetric array, then, is the same as for a single microprobe. Feedback to individual SQUID sensors compensates residual asymmetry of an array.

The remaining principal problem facing development of a microprobe is its cryogenic structure. Design of the cryogenic structure poses two main problems. The first is to achieve a spacing of 1 mm or so between the pickup coils and a test surface. The second is to attach the probe with a cryogenic umbilical to a remote cryostat housing SQUID sensors. The first requirement is essential for high performance; the second makes it convenient to scan test samples.

Radiant heat tranfer from a polished surface at 300 K, with an emissivity of 0.03, to one at 4 K is about 0.007 mW/(mm)^2, so the radiant heat load on the tip of a microprobe 4 mm in radius is about 0.35 mW. A copper wire 1 mm in radius, with a thermal conductivity of about 1 W/cm/K at 4 K, requires a temperature difference of 1 K over a length of 100 cm to transport a heat load of 0.35 mW. Consequently, fine copper wire in a flexible, stainless steel vacuum jacket, which is superinsulated, can provide a cyrogenic umbilical cord one meter or so long that links the microprobe tip to a cryostat containing liquid helium.

At the tip of the microprobe is a thin sapphire window that allows a 1 mm spacing between the pickup coils and a test surface. A point contact fixes pickup coils in the tip to prevent relative motion from thermal contraction during cooling to 4 K. Differential contraction is taken up by slack in the copper wire that thermally grounds the tip to the helium reservoir in the cryostat. The cryostat houses the SQUID sensor and is a conventional design that uses thermal shields cooled by helium vapor. A probe that fits down the central tube of the cryostat immerses the sensor in the helium reservoir. An umbilical cord leads out from the top of the cryostat probe and enables readily scanning surfaces with a microprobe.

We expect ac losses, which depend on wire characteristics and operating frequency, from a current of one ampere in the superconducting drive coils to contribute a few milliwatts to the heat load on the umbilical cord, which would increase its temperature differential by several degrees Kelvin. The increase can be enough to exceed the critical temperature of niobium, even though helium loss is acceptable (a loss of one liter of liquid per day requires 30 mW). Operating at drive currents of a few amperes and frequencies of several thousand Hertz could increase the heat load tenfold. It would require tripling the the diameter of copper wire in the umbilical cord or using a cryogenic heat pipe (Chi and Cygnarowicz, 1970) to obtain a smaller diameter structure with thermal conductance tenfold greater than copper.

6.2 TECHNICAL RISK

Technology of niobium SQUIDs enables development of a microprobe. Reliable sensors are commercially available. The main technical risk is in meeting performance goals and developing a cryogenic design that makes an electromagnetic microscope a versatile research tool. Almost certainly, a first probe design falls short of anticipated performance and utility, but an iterative development plan can advance design of a microprobe and increase its performance and utility in sequential stages. The plan minimizes risks in meeting performance goals.

Cryogenic, mechanical, and electronics designs present the main risk factors in development. Mechanical and electronics design are critical elements that determine performance and so present the greatest risk. Cryogenic design mainly determines utility of a microprobe but also can affect its performance.

Mechanical and electronic design set performance limits of a microprobe. Suppressing interference and noise of a microprobe requires precise mechanical design and machining. Electronic feedback nulls interference that remains because of limits to mechanical precision. It requires high quality electronics to null residual interference and to maintain a stable operating point with minimal drift and harmonic contamination. To achieve high performance, combined mechanical precision and electronic feedback must reduce interference by a factor of 10^7 to 10^8, with mechanical precision contributing a factor of 10^3 to 10^4. The required suppression of interference falls within practical limits of high quality mechanics and electronics and so presents a moderate risk to achieving high

performance.

Development of a cryogenic umbilical to thermally ground a microprobe to a cryostat housing SQUID sensors enhances utility of a microprobe and sets a secondary limit on its performance. Use of copper wire to transport heat in an umbilical presents a moderate risk, but it could limit performance of large arrays of microprobes. Use of a helium filled heat pipe to transport heat would remove performance limits for large arrays, but it presents a higher risk, because it is a new cryogenic technique.

Overall technical risk of developing high peformance microprobes and using them to form the magnetic eye of an electromagnetic microscope is moderate.

7.0 CONCLUSION

High performance microprobes hold the promise of forming the magnetic eye of an electromagnetic microscope that promises high resolution, wide field of view, and large depth of field for imaging internal flaws in aluminum. A current of 1 A oscillating at a few kilohertz in drive coils a few millimeters in radius together with coplanar receiver loops 1 mm or less in radius form a high performance microprobe. A microprobe with a receiver forming a gradiometer of fourth order gives a field of view of about 5 mm and a horizontal resolution of about 1 mm to a 0.1 mm flaw at a depth of a few millimeters. A receiver forming a gradiometer of second order gives a field of view of 12 mm or so and a horizontal resolution of about 3 mm at a depth of field of 8 mm.

Closely packed microprobes arrayed in parallel rows form the eye of a electromagnetic microscope. The eye gives multiple images of an internal flaw, one for each row or pair of rows, that can resolve depth of a 0.1 mm flaw to a few tenths of a millimeter together with a horizontal resolution of 1 mm or so. Cryogenic umbilicals connect the eye to a remote cryostat housing SQUID sensors to provide ease of scanning and make it a versatile tool.

8.0 REFERENCES

Bain, R.J.P., Donaldson, G.B., Evanson, S., and Hayward, G., Design and Operation of SQUID–based Planar Gradiometers for Non–destructive Testing of Ferromagnetic Plates, IEEE Trans. on Magnetics, MAG–23, 473–476, 1987.

Burrows, M. L., A Theory of Eddy Current Flaw Detection, University of Michigan, Ph.D. thesis, 1964, University Microfilms, Inc., Ann Arbor, Mich..

Chi, S.W. and Cygnarowicz, T. A., Theoretical Analyses of Cryogenic Heat Pipes, Space Technology and Heat Transfer Conf., Los Angeles, Calif., 1970.

Czipott, P.V. and Podney, W.N., Use of a Superconductive Gradiometer in an Ultrasensitive Electromagnetic Metal Detector, IEEE Trans. on Magnetics, MAG–25, No. 2, 1204–1207, 1989.

Dodd, C. V., Deeds, W. E., and Luquire, J. W., Integral Solutions to Some Eddy Current Problems, Int. J. of Nondestructive Testing, 1, 29–90, 1969.

Evanson, S., Bain, R.J.P., Donaldson, G.B., Stirling, G., and Hayward, G., A Comparison of the Performance of Planar and Conventional Second–Order Gradiometers Coupled to a SQUID for the NDT of Steel Plates, IEEE Trans. on Magnetics, MAG–25, No. 2, p. 1200–1203, 1989.

Fickett, F.R. and Capobianco, T.E., NBS Work in SQUID–basesd NDE, SQUID/NDE Workshop, Harper's Ferry, West Virginia, 1988.

Gradshteyn, I.S. and Ryzhik, I.M., Table of Integrals, Series, and Products, Academic Press, New York, 1980.

Kraichman, M.B., Handbook of Electromagnetic Propagation in Conducting Media, *Navmat* P–2302, U.S. Govt. Printing Office, Washington, D.C., 1970.

Krampfner, Y.D. and Johnson, D.D., Flexible Substrate Eddy Current Coil Arrays, Rev. of Progress in Quantitative Nondestructive Evaluation, Vol. 7A, Ed. D.O. Thompson and D.E. Chimenti, Plenum Press, New York, p 471–478, 1988.

Panofsky, W.K.H. and Phillips, M., Classical Electricity and Magnetism, Addison–Wesley Publishing Co., Inc., Reading, Massachusetts, 1962.

Roth, B.J., Sepulveda, N.G., and Wikswo, J.P., Using a Magnetometer to Image a Two–dimensional Current Distribution, J. Appl. Phys., 65(1), 361–372, 1989.

Smythe, W.R., Static and Dynamic Electricity, McGraw–Hill Book Company, New York, 1968

Weinstock, H., Erber, T., and Nisenoff, M., Threshold of Barkhausen Emission and Onset of Hysteresis in Iron, Phys. Rev. B, 31, No. 3, 1535–1553, 1985.

Weinstock, H. and Nisenoff, M., Nondestructive Evaluation of Metallic Structures Using a SQUID Magnetometer, SQUID '85, Ed., H.D. Hahlbohm, H. Lubbig, Walter de Gruyter & Co., Berlin, p854–858, 1985.

APPENDIX A

EDDY CURRENTS IN A UNIFORMLY CONDUCTING HALF–SPACE FROM AN ELECTRIC CURRENT OSCILLATING IN A CIRCULAR LOOP

Appendix A describes eddy currents induced in a half–space of uniform electrical conductivity, σ, by electric current oscillating in a circular loop at height h above the surface of the half–space. The axis of the loop of radius r_0 is normal to the surface.

We use Ampere's law together with Faraday's law to formulate a description of induced currents and fields in terms of a vector potential, $\vec{A}$, of magnetic flux density, $\vec{B}$. We express the vector potential in terms of two scalar potentials and obtain solutions for them in terms of Fourier integrals in cylindrical coordinates r, ϕ, and z, where the $\hat{z}$ axis points along the axis of the current loop. Scalar potentials give so–called transverse electric and transverse magnetic type fields. Source currents flowing tangential to the surface of the half–space generate transverse electric type fields, and source currents flowing normal to the surface generate transverse magnetic type fields.

A.1 FORMULATION

Ampere's law in the form

$$\vec{\nabla} \times \vec{H} = \vec{J} + \vec{J}_s \qquad \text{(A1.a)}$$

together with the constituent relation, $\vec{B} = \mu_0 \vec{H}$ with $\mu_0 = 4\pi \times 10^{-7}$ H/m , and Ohm's law, $\vec{J} = \sigma \vec{E}$, relate magnetic flux density to electric field, $\vec{E}$, induced by an imposed, oscillating current of density $\vec{J}_s$. Faraday's law, expressed by the relation

$$\vec{\nabla} \times \vec{E} = -\partial \vec{B}/\partial t \,, \qquad \text{(A1.b)}$$

closes the formulation by relating the induced electric field to a changing density of magnetic flux, $\vec{B}$.

Equations A1.a and A1.b tell us that a solenoidal vector potential, $\vec{\nabla} \cdot \vec{A} = 0$, satisfies the relation

$$\nabla^2 \vec{A} - \mu_0 \sigma \, \partial \vec{A}/\partial t = -\mu_0 \vec{J}_s \,, \qquad \text{(A2)}$$

where $\vec{B} = \vec{\nabla} \times \vec{A}$ and $\vec{E} = -\partial \vec{A}/\partial t$. Equation A2 together with continuity of tangential components of electric and magnetic fields across boundaries give the vector potential for a specified source current.

A.2 SCALAR POTENTIALS

Because the vector potential is solenoidal, we express it as the curl of a second vector potential, $\vec{Z}$, composed of two scalar potentials Z_1 and Z_2 ; namely, (Smythe, 1969)

$$\vec{Z} = Z_1 \hat{z} + \vec{\nabla} \times Z_2 \hat{z} \ , \tag{A3.a}$$

where

$$\vec{A} = \mu_0 \vec{\nabla} \times \vec{Z} \ . \tag{A3.b}$$

Equations A3.a and A3.b tell us that the relations

$$\vec{E} = \partial/\partial t \ [\ \hat{z} \times \vec{\nabla} Z_1 + \hat{z} \ \nabla^2 Z_2 - \vec{\nabla}(\hat{z} \cdot \vec{\nabla} Z_2) \ ] \tag{A3.c}$$

and

$$\vec{H} = \hat{z} \times \vec{\nabla}(\nabla^2 Z_2) - \hat{z} \ \nabla^2 Z_1 + \vec{\nabla}(\hat{z} \cdot \vec{\nabla} Z_1) \tag{A3.d}$$

give electric and magnetic fields in terms of scalar potentials. Equation A3.c says that the scalar potential Z_1 gives an electric field that is transverse to the $\hat{z}$ axis, a so–called transverse electric type field, and Equation A3.d says that the scalar potential Z_2 gives a transverse magnetic type field.

We find from Equations A2 and A3.b that the vector potential $\vec{Z}$ satisfies the relation

$$\nabla^2 \vec{Z} - \mu_0 \sigma \ \partial \vec{Z}/\partial t = - \vec{M}_s \ , \tag{A4.a}$$

where $\vec{M}_s$ is the magnetization density of the source; namely,

$$\vec{J}_s = \vec{\nabla} \times \vec{M}_s \ . \tag{A4.b}$$

Because the source current is solenoidal, we can express source magnetization in terms of two scalar components, M_1 and M_2, as

$$\vec{M}_s = M_1 \hat{z} + \vec{\nabla} \times M_2 \hat{z} \ , \tag{A5.a}$$

so

$$\vec{J}_s = - \hat{z} \times \vec{\nabla} M_1 - \hat{z} \ \nabla^2 M_2 + \vec{\nabla}(\hat{z} \cdot \vec{\nabla} M_2) \ . \tag{A5.b}$$

The component M_1 gives electric currents transverse to $\hat{z}$. A current along $\hat{z}$ requires a transverse component of magnetization, expressed by M_2.

Equations A3.a and 4.a then tell us that the scalar potentials Z_1 and Z_2 satisfy the relation

$$\nabla^2 Z_i - \mu_0 \sigma \ \partial Z_i/\partial t = - M_i \ , \tag{A6}$$

with $i = 1, 2$. Equation A6 tells us that the scalar source magnetization M_1 excites a transverse electric type field and that M_2 excites a transverse magnetic type field. Consequently, a source current transverse to the $\hat{z}$ axis excites a transverse electric type field, specified by the scalar potential Z_1, and a current along the $\hat{z}$ axis excites a transverse magnetic type field, specified by the scalar component Z_2 alone. Current flowing in a circular loop parallel to the surface of a half–space, then, excites a transverse electric type field alone.

A.3 TRANSVERSE ELECTRIC TYPE FIELD OF A CIRCULAR CURRENT

The relation

$$\vec{J}_s = \hat{\phi}\, I\, \delta(r-r_o)\, \delta(z-h) \tag{A7.a}$$

expresses the current density in a circular loop of radius r_o that carries a current I in direction $\hat{\phi}$ at height h above the surface of a half–space. Dirac delta functions, $\delta(x)$, express localization of the current. Equation A5.b tells us that the relation

$$\vec{M}_s = -\hat{z}\, I\, \mathcal{H}(r-r_o)\, \delta(z-h) \tag{A7.b}$$

gives the corresponding density of magnetization, where $\mathcal{H}(x)$ is a Heaviside step function. Consequently, fields of the current loop are a transverse electric type, so

$$\vec{E} = i\omega\, \hat{z} \times \vec{\nabla} Z_1 \tag{A7.c}$$

and

$$\vec{H} = -\hat{z}\, \nabla^2 Z_1 + \vec{\nabla}(\hat{z}\cdot\vec{\nabla} Z_1) \tag{A7.d}$$

for a current oscillating at frequency ω.

Equation A6 then tells us that the expressions

$$\nabla^2 Z_1^a = I\, \mathcal{H}(r-r_o)\, \delta(z-h) \quad , \text{for } z > 0, \tag{A8.a}$$

and

$$\nabla^2 Z_1^c - i\omega\, \mu_o \sigma\, Z_1^c = 0 \quad , \text{for } z < 0, \tag{A8.b}$$

specify a scalar potential above the surface, Z_1^a, and within the conducting half–space, Z_1^c. Continuity of tangential components of electric and magnetic fields at $z = 0$ requires that Z_1 and its derivative $\partial Z_1/\partial z$ be continuous across the surface; namely, that $Z_1^a = Z_1^c$ and $\partial Z_1^a/\partial z = \partial Z_1^c/\partial z$ at $z = 0$. Equations 8.a and 8.b together with continuity required at the boundary determine the scalar potentials Z_1^a and Z_1^c. We express the potentials in terms of Fourier integrals.

A.3.1 Fourier Integrals

The integral

$$Z(\vec{r},z) = \iint_{-\infty}^{\infty} \tilde{Z}(\vec{k},z)\, e^{-i\vec{k}\cdot\vec{r}}\, d\vec{k} \quad , \tag{A9.a}$$

where

$$\tilde{Z}(\vec{k},z) = (2\pi)^{-2} \iint_{-\infty}^{\infty} Z(\vec{r},z)\, e^{i\vec{k}\cdot\vec{r}}\, d\vec{r} \quad , \tag{A9.b}$$

expresses a function $Z(\vec{r},z)$ in terms of its Fourier transform $\tilde{Z}(\vec{k},z)$ over a radial vector $\vec{r}$. From Equations A8.a and A8.b, we then find that the expressions

$$\frac{d^2\tilde{Z}_1^a}{dz^2} - k^2\,\tilde{Z}_1^a = \frac{-Ir_o\, J_1(kr_o)}{2\pi k}\,\delta(z-h) \quad , \text{for } z > 0, \tag{A9.c}$$

and

$$\frac{d^2\tilde{Z}_1^c}{dz^2} - \gamma^2\,\tilde{Z}_1^c = 0 \quad , \text{for } z < 0, \tag{A9.d}$$

together with continuity requirements at $z = 0$, $\tilde{Z}_1^a = \tilde{Z}_1^c$ and $d\tilde{Z}_1^a/dz = d\tilde{Z}_1^c/dz$, specify Fourier transforms of the scalar potential Z_1, where $\gamma^2 = k^2 + i\omega\mu_o\sigma$.

We use Equations A9.c and A9.d to find that the expressions

$$\tilde{Z}_1^a(k,z) = \frac{Ir_o\, J_1(kr_o)}{4\pi\, k^2}\left[e^{-k|z-h|} + \frac{(1-\gamma/k)}{(1+\gamma/k)}\, e^{-k(z+h)}\right] \tag{A10.a}$$

and

$$\tilde{Z}_1^c(k,z) = \frac{Ir_o\, J_1(k\,r_o)}{2\pi\, k^2(1+\gamma/k)}\, e^{\gamma z - kh} \tag{A10.b}$$

give the transforms $\tilde{Z}_1^a$, for $z > 0$ and $\tilde{Z}_2^c$, $z < 0$. The integrals

$$Z_1^a(r,z) = \frac{Ir_o}{2}\int_0^{\infty} \left[e^{-k|z-h|} + \frac{(1-\gamma/k)}{(1+\gamma/k)}\, e^{-k(z+h)}\right] J_1(kr_o)\, J_o(kr)\, dk/k \tag{A10.c}$$

and

$$Z_1^c(r,z) = Ir_o \int_0^{\infty} \left[\frac{e^{\gamma z - kh}}{1+\gamma/k}\right] J_1(kr_o)\, J_o(kr)\, dk/k \tag{A10.d}$$

give corresponding scalar potentials. Here, the relation

$$\frac{\gamma}{k} = \frac{1}{\sqrt{2}}\left\{ \sqrt{1 + \sqrt{1+4/(\delta k)^2}} + i\sqrt{\sqrt{1+4/(\delta k)^2} - 1}\right\} \tag{A10.e}$$

expresses the complex ratio γ/k in terms of the skin depth $\delta = \sqrt{2/(\mu_o\sigma\omega)}$.

A.3.1 Vector Potential

From the relation

$$\vec{A} = \mu_o \vec{\nabla} \times \vec{Z} = -\hat{\phi}\, \mu_o\, \partial Z_1/\partial r \qquad \text{(A11.a)}$$

and Equations A10.c and A10.d, we find that the expressions

$$\vec{A}_a(r,z) = \vec{A}_o(r,z) + \frac{\mu_o I r_o}{2} \hat{\phi} \int_0^\infty \frac{(1-\gamma/k)}{(1+\gamma/k)} e^{-k(z+h)}\, J_1(kr_o)\, J_1(kr)\, dk \qquad \text{(A11.b)}$$

and

$$\vec{A}_c(r,z) = \mu_o I r_o \hat{\phi} \int_0^\infty \left[\frac{e^{\gamma z - kh}}{1+\gamma/k}\right] J_1(kr_o)\, J_1(kr)\, dk \qquad \text{(A11.c)}$$

give the vector potential $\vec{A}_a$, for $z > 0$ and $\vec{A}_c$, for $z < 0$. For low frequencies and or low conductivity, $\gamma \approx k$ and $\vec{A}_a \approx \vec{A}_c \approx \vec{A}_o$, where $\vec{A}_o$ is the vector potential of a loop in free space; namely,

$$\vec{A}_o(r,z) = \frac{\mu_o I r_o}{2} \hat{\phi} \int_0^\infty e^{-k|z-h|}\, J_1(kr_o)\, J_1(kr)\, dk \ , \qquad \text{(A11.d)}$$

or (Smythe, 1969)

$$\vec{A}_o(r,z) = \frac{\mu_o I}{\pi\rho}\sqrt{\frac{r_o}{r}} \left[(1-\rho^2/2)\, K(\rho) - E(\rho)\right] \hat{\phi} \ , \qquad \text{(A11.e)}$$

where $K(\rho)$ and $E(\rho)$ are, respectively, complete elliptic integrals of the first and second kinds and $\rho^2 = 4rr_o/[(z-h)^2+(r+r_o)^2]$. Equations A11.b and A11.c expressing the vector potential agree with expression given by Dodd, Deeds, and Luquire, 1969.

A.3.2 Electric Field and Eddy Currents

The relation

$$\vec{E}(r,z) = -i\omega \{\ \mathcal{H}(z)\, \vec{A}_a(r,z) + [1-\mathcal{H}(z)]\, \vec{A}_c(r,z)\ \} \qquad \text{(A12.a)}$$

gives the corresponding electric field, where $\mathcal{H}(z)$ denotes a Heaviside step function, and the relation

$$\vec{J}(r,z) = -i\omega\sigma\, \vec{A}_c(r,z) \qquad \text{(A12.b)}$$

gives eddy currents induced in the conducting half–space, $z < 0$.

A.3.3 Magnetic Flux Density

The relations

$$B_r(r,z) = B_{ro}(r,z) + \frac{\mu_o I r_o}{2}\int_0^\infty \frac{(1-\gamma/k)}{(1+\gamma/k)} e^{-k(z+h)} J_1(kr_o)\, J_1(kr)\, k\, dk \qquad \text{(A13.a)}$$

and

$$B_z(r,z) = B_{zo}(r,z) + \frac{\mu_o I r_o}{2}\int_0^\infty \frac{(1-\gamma/k)}{(1+\gamma/k)} e^{-k(z+h)} \Big] J_1(kr_o)\, J_0(kr)\, k\, dk \qquad \text{(A13.b)}$$

give respective radial and vertical components of the density of magnetic flux for $z > 0$, and the relations

$$B_r(r,z) = -\mu_o I r_o \int_0^\infty \left[\frac{\gamma/k}{1+\gamma/k}\right] e^{\gamma z - kh} J_1(kr_o)\, J_1(kr)\, k\, dk \qquad \text{(A13.c)}$$

and

$$B_z(r,z) = \mu_o I r_o \int_0^\infty \left[\frac{1}{1+\gamma/k}\right] e^{\gamma z - kh} J_1(kr_o)\, J_0(kr)\, k\, dk \qquad \text{(A13.d)}$$

give the components for $z < 0$. Here, B_{ro} and B_{zo} are respective radial and vertical components of the magnetic flux density of a loop in free space; namely,

$$B_{ro}(r,z) = \frac{\mu_o I}{2\pi r}\frac{(z-h)}{\sqrt{(r+r_o)^2+(z-h)^2}}\left[\frac{r^2+r_o^2+(z-h)^2}{(r_o-r)^2+(z-h)^2} E(\rho) - K(\rho)\right] \qquad \text{(A13.e)}$$

and

$$B_{zo}(r,z) = \frac{\mu_o I}{2\pi}\frac{1}{\sqrt{(r+r_o)^2+(z-h)^2}}\left[\frac{r_o^2-r^2-(z-h)^2}{(r_o-r)^2+(z-h)^2} E(\rho) + K(\rho)\right], \qquad \text{(A13.f)}$$

where again $K(\rho)$ and $E(\rho)$ are, respectively, complete elliptic integrals of the first and second kinds and $\rho^2 = 4rr_o/[(z-h)^2+(r+r_o)^2]$.

APPENDIX B

MUTUAL INDUCTANCES OF COAXIAL LOOPS ABOVE A CONDUCTING HALF–SPACE

Appendix B uses the vector potential derived in Appendix A to give an expression for the mutual inductance of two coaxial loops above a conducting half–space. Mutual inductance of a pair of loops, M_{ij} , is the magnetic flux threading one loop as a result of a unit electric current flowing in the other loop.

For coaxial, circular loops with radii r_i and r_j and corresponding numbers of turns N_i and N_j , the expression

$$M_{ij} = N_i r_i N_j \int_0^{2\pi} \hat{\phi} \cdot \vec{A}_j(r_i,h_i)\, d\phi \qquad \text{(B1)}$$

gives the flux threading the *ith* loop for unit current flowing in the *jth* loop, where $\vec{A}_j$ is the vector potential of current in the *jth* loop. It is evaluated at the radius and height, r_i and h_i , of the *i*th loop. Integration in Equation B1 extends over the azimuthal coordinate ϕ of cylindrical coordinates r, ϕ, and z measured from the axis of the coaxial loops. For coaxial, circular loops, the vector potential is azimuthally symmetric and points along the unit vector $\hat{\phi}$, so integration simply gives a factor of 2π .

Equation A11.b of Appendix A gives the vector potential $\vec{A}_j(r,h)$, $h>0$, of a current $I_j\hat{\phi}$ flowing in a circular loop of radius r_j at height h_j above a conducting half–space; namely,

$$\vec{A}_j(r,h) = \vec{A}_j^{\circ}(r,h) + \frac{\mu_o I_j r_i}{2}\,\hat{\phi} \int_0^{\infty} \frac{(1-\gamma/k)}{(1+\gamma/k)}\, e^{-k(h+h_j)}\, J_1(kr)\, J_1(kr_j)\, dk \ . \qquad \text{(B2.a)}$$

Here, $\vec{A}_j^{\circ}$ is the vector potential of the loop in free space; namely,

$$\vec{A}_j^{\circ}(r,h) = \frac{\mu_o I_j r_i}{2}\,\hat{\phi} \int_0^{\infty} e^{-k|h-h_j|}\, J_1(kr)\, J_1(kr_j)\, dk \ , \qquad \text{(B2.b)}$$

or (Smythe, 1969)

$$\vec{A}_j^{\circ}(r,h) = \frac{\mu_o I_j}{\pi\rho_j}\sqrt{\frac{r_i}{r}}\left[(1-\rho_j^2/2)\, K(\rho_j) - E(\rho_j)\right]\hat{\phi} \ , \qquad \text{(B2.c)}$$

where $K(\rho_j)$ and $E(\rho_j)$ are, respectively, complete elliptic integrals of the first and second kinds and $\rho_j^2 = 4rr_j/[(h-h_j)^2+(r+r_j)^2]$.

Equations B1 and B2.a, with $I_j = 1$, then tell us that the expression

$$M_{ij} = M^o_{ij} + \pi\mu_o\, N_i r_i\, N_j r_j \int_0^\infty \frac{(1-\gamma/k)}{(1+\gamma/k)}\, e^{-k(h_i+h_j)}\, J_1(kr_i)\, J_1(kr_j)\, dk \qquad \text{(B3.a)}$$

gives the mutual inductance of a pair of coaxial loops of radii r_i and r_j and corresponding numbers of turns N_i and N_j at heights h_i and h_j above a conducting half–space. Here, M^o_{ij} is the mutual inductance of the loops in free space; namely,

$$M^o_{ij} = \pi\mu_o\, N_i r_i\, N_j r_j \int_0^\infty e^{-k|h_i-h_j|}\, J_1(kr_i)\, J_1(kr_j)\, dk \ , \qquad \text{(B3.b)}$$

or

$$M^o_{ij} = \mu_o N_i N_j\, [(h_i-h_j)^2 + (r_i+r_j)^2] \left[(1-\rho_{ij}^2/2)\, K(\rho_{ij}) - E(\rho_{ij})\right] \ , \qquad \text{(B3.c)}$$

where again $K(\rho_{ij})$ and $E(\rho_{ij})$ are, respectively, complete elliptic integrals of the first and second kinds and $\rho_{ij}^2 = 4r_ir_j/[(h_i-h_j)^2+(r_i+r_j)^2]$. Equation B3.a says that $M_{ij} = M_{ji}$, as required by reciprocity.

For coplanar loops at height h above the surface, $h_i = h_j = h$, so Equation B3.a says that

$$M_{ij}(h) = M^{oo}_{ij} + \pi\mu_o\, N_i r_i\, N_j r_j \int_0^\infty \frac{(1-\gamma/k)}{(1+\gamma/k)}\, e^{-2kh}\, J_1(kr_i)\, J_1(kr_j)\, dk \ , \qquad \text{(B4.a)}$$

where

$$M^{oo}_{ij} = \pi\mu_o\, N_i r_i\, N_j r_j \int_0^\infty J_1(kr_i)\, J_1(kr_j)\, dk \ , \qquad \text{(B4.b)}$$

or (Gradshteyn and Ryshik, 1980)

$$M^{oo}_{ij} = \mu_o N_i N_j\, (r_i+r_j)^2 \left\{[1-(\rho^o_{ij})^2/2]\, K(\rho^o_{ij}) - E(\rho^o_{ij})\right\} \ , \qquad \text{(B4.c)}$$

where $(\rho^o_{ij})^2 = 4r_ir_j/(r_i+r_j)^2$.

APPENDIX C

RECIPROCITY RELATION

Appendix C develops a reciprocity relation between a vector potential $\vec{A}_i$ that results from a source current $\vec{J}_{si}$ and a vector potential $\vec{A}_j$ that arises from a source current $\vec{J}_{sj}$. We use the vector identity (Gradshteyn and Ryzhik, 1980)

$$\vec{\nabla}\cdot(\vec{A}_i \times \vec{H}_j) = \vec{H}_j\cdot\vec{\nabla} \times \vec{A}_i - \vec{A}_i\cdot\vec{\nabla} \times \vec{H}_j \qquad \text{(C1.a)}$$

together with Ampere's law in the form

$$\vec{\nabla} \times \vec{H}_j = \vec{J}_j + \vec{J}_{sj} \qquad \text{(C1.b)}$$

and the constituent relation

$$\vec{B}_j = \mu_0(\vec{H}_j + \vec{M}_j) \ , \qquad \text{(C1.c)}$$

where $\vec{J}_j$ is an induced conduction current, $\vec{M}_j$ is magnetization, and the relations $\vec{B}_j = \vec{\nabla} \times \vec{A}_j$ and $\vec{J}_j = -\sigma\, \partial A_j/\partial t$ respectively express density of magnetic flux, $\vec{B}_j$, and induced current, $\vec{J}_j$, in terms of a vector potential, $\vec{A}_j$. We find from Equations C1.a, C1.b, and C1.c that the expression

$$\vec{\nabla}\cdot(\vec{A}_i \times \vec{H}_j - \vec{A}_j \times \vec{H}_i) = \mu_0(\vec{H}_j\cdot\vec{M}_i - \vec{H}_i\cdot\vec{M}_j) - \sigma\left[\vec{A}_j\cdot\frac{\partial\vec{A}_i}{\partial t} - \vec{A}_i\cdot\frac{\partial\vec{A}_j}{\partial t}\right] + \vec{A}_j\cdot\vec{J}_{si} - \vec{A}_i\cdot\vec{J}_{sj} \qquad \text{(C1.d)}$$

relates fields from the current sources $\vec{J}_{si}$ and $\vec{J}_{sj}$.

For sinusoidal current oscillations in a linear, isotropic medium, the terms in Equation C1.d that come from magnetization and induced currents vanish because of symmetry, so

$$\vec{\nabla}\cdot(\vec{A}_i \times \vec{H}_j - \vec{A}_j \times \vec{H}_i) = \vec{A}_j\cdot\vec{J}_{si} - \vec{A}_i\cdot\vec{J}_{sj} \ . \qquad \text{(C2.a)}$$

For confined current sources, fields vanish at infinity, so the intergral of their divergence over all space vanishes as well. Equation C2.a then says that the expression

$$\int \vec{A}_j\cdot\vec{J}_{si}\, d\vec{v} = \int \vec{A}_i\cdot\vec{J}_{sj}\, d\vec{v} \qquad \text{(C2.b)}$$

gives a reciprocity relation between vector potentials and impressed current densities, where intergrals extend over volumes of respective current sources.

For filamentary source currents in circuits i and j, Equation C2.b says that the magnetic flux threading circuit i from unit current in circuit j equals the magnetic flux threading circuit j from unit current in circuit i. Namely, mutual inductance between the circuits is symmetric. The integral expression extends symmetry of mutual inductance to volumetric current sources.